Sensory axons induce epithelial lipid microdomain remodeling and determine the distribution of junctions in the epidermis

Jeffrey B. Rosa[†,*], Khaled Y. Nassman, and Alvaro Sagasti[*]
Department of Molecular, Cell and Developmental Biology and Molecular Biology Institute, University of California, Los Angeles, Los Angeles, CA 90095

ABSTRACT **Epithelial cell properties are determined by the polarized distribution of membrane lipids, the cytoskeleton, and adhesive junctions. Epithelia are often profusely innervated, but little work has addressed how neurites affect epithelial organization. We previously found that basal keratinocytes in the zebrafish epidermis enclose axons in ensheathment channels sealed by autotypic junctions. Here we characterized how axons remodel cell membranes, the cytoskeleton, and junctions in basal keratinocytes. At the apical surface of basal keratinocytes, axons organized lipid microdomains quantitatively enriched in reporters for PI(4,5)P2 and liquid-ordered (Lo) membranes. Lipid microdomains supported the formation of cadherin-enriched, F-actin protrusions, which wrapped around axons, likely initiating ensheathment. In the absence of axons, cadherin-enriched microdomains formed on basal cells but did not organize into contiguous domains. Instead, these isolated domains formed heterotypic junctions with periderm cells, a distinct epithelial cell type. Thus, axon endings dramatically remodel polarized epithelial components and regulate epidermal adhesion.**

Monitoring Editor
Julie Brill
The Hospital for Sick Children

Received: Sep 6, 2022
Revised: Oct 21, 2022
Accepted: Oct 25, 2022

INTRODUCTION

Epithelia line all of our organs, cavities, and body surfaces, regulating exchange with the outside environment and serving as protective barriers. To carry out these functions, epithelial cells must build polarized membrane domains facing the outside (apical) and inside (basal) environments. Distinct lipids and proteins segregate to apical and basal-lateral membranes, making them biochemically distinct and promoting the formation of polarized structures, including cytoskeletal protrusions and junctions, which join cells into coherent sheets. Junctions also provide instructive polarity cues, enable the generation of specific tissue shapes, impart mechanical strength to tissues, and initiate signaling that responds to the biochemical and mechanical state of the epithelium. Although often overlooked, most epithelia are profusely innervated by sensory or sympathetic neurons. Little work has addressed how neurite growth among epithelial cells affects the polarized organization of epithelial components.

The outer epithelial layer of the skin, the epidermis, serves as both a barrier and a sensory organ. Afferent neurites of sensory neurons innervate the epidermis to mediate nociception—the detection of painful mechanical, chemical, or thermal stimuli (Zylka *et al.*, 2005). In mammals, the "free" axonal nerve endings of pain-sensing trigeminal and dorsal root ganglia neurons branch extensively in the epidermis, forming immense receptive fields (Wu *et al.*, 2012). Although free nerve endings do not contact specialized skin structures (Zylka *et al.*, 2005), recent evidence indicates that these axon endings are functionally coupled (Sondersorg *et al.*, 2014; Baumbauer *et al.*, 2015; Pang *et al.*, 2015; Moehring *et al.*, 2018; Mikesell *et al.*, 2022; Yoshino *et al.*, 2022): Chemo- or optogenetic activation of keratinocytes promotes sensory afferent firing and nocifensive behaviors, while electrically silencing keratinocytes attenuates these behaviors. It has even been suggested that keratinocytes and free nerve endings form synapse-like contacts with one another

This article was published online ahead of print in MBoC in Press (http://www.molbiolcell.org/cgi/doi/10.1091/mbc.E22-09-0396) on November 2, 2022.

Conflict of interest: The authors declare that they have no conflict of interest.

[†]Present address: Department of Psychiatry, University of Pennsylvania Perelman School of Medicine, 415 Curie Blvd., Philadelphia, PA, 19104.

*Address correspondence to: Jeffrey B. Rosa (jeffro@pennmedicine.upenn.edu); Alvaro Sagasti (sagasti@mcdb.ucla.edu).

Abbreviations used: AAD, axon-associated membrane domain; BAC, bacterial artificial chromosome; dpf, days post-fertilization; gg, geranylgeranylated; GPI, glycosylphosphatidylinositol; hpf, hours post-fertilization; Ld, liquid-disordered; Lo, liquid-ordered; MO, morpholino; mp, myrpalm (myristoylated and palmitoylated); PIP2, phosphatidylinositol 4,5-bisphosphate; PLCδ-PH, pleckstrin homology domain of phospholipase C-δ1; ROI, region.

(Talagas *et al.*, 2020a). Investigating how free nerve endings initiate and maintain contact with keratinocytes is thus essential for understanding the development of the epidermis and its pain-sensing functions.

While much is known about skin-derived signals that attract and pattern peripheral axon arbors (Yin *et al.*, 2021), less attention has been paid to how neurites interact with skin cells once in the epidermis. In both invertebrates and vertebrates, a subset of cutaneous sensory neurons become enveloped by epithelial cell membranes into ensheathment channels, which may be sealed by autotypic epithelial junctions (O'Brien *et al.*, 2012; Tenenbaum *et al.*, 2017; Jiang *et al.*, 2019; Talagas *et al.*, 2020b) or simply engulfed by epidermal membranes (Chalfie and Sulston, 1981). Epidermal ensheathment regulates neurite branching (Tenenbaum *et al.*, 2017; Jiang *et al.*, 2019), determines neurite arbor spacing in the skin (Han *et al.*, 2012; Kim *et al.*, 2012; Yang *et al.*, 2019), protects neurites from physical damage (Coakley *et al.*, 2020), and is required for efficient sensory function (Jiang *et al.*, 2019).

In flies and zebrafish, the earliest known step in epidermal ensheathment is the accumulation of membranes enriched in a biosensor for the phosphoinositide PI(4,5)P2 (PIP2) at the neurite–skin cell interface (Jiang *et al.*, 2019), indicating that this membrane region has either a distinct lipid composition or greater membrane density. These regions then recruit F-actin in a Rho1-dependent manner (Jiang *et al.*, 2019), presumably to promote curvature of the epidermal membrane to enwrap the neurite. Finally, junction proteins are recruited to seal the neurites within ensheathment channels (O'Brien *et al.*, 2012; Jiang *et al.*, 2019). This sequence of changes in epidermal cell membranes requires the presence of neurites (Jiang *et al.*, 2019), indicating that cues from neurites signal to the skin cell to initiate the ensheathment process. Because most epithelial cells contact many sensory neurites, the formation of autotypic junctions at ensheathment channels has the potential to dramatically redistribute membrane, cytoskeletal components, and junctions in epithelial cells, potentially impacting junction-associated signaling and adhesion.

In diverse cellular contexts, membrane domains with distinct lipid compositions function as platforms for signaling and cell–cell interactions. For example, cholesterol and sphingolipids are not distributed uniformly in the plasma membrane but rather are enriched in domains with lower membrane fluidity, owing to tight packing of the sterol rings on cholesterol with long, saturated acyl chains of sphingolipids (Garcia-Parajo *et al.*, 2014). In simplified model membranes, cholesterol and sphingolipids undergo large-scale phase separation into micron-sized domains called liquid-ordered (Lo) domains, sometimes equated with lipid "rafts," which are distinct from so-called liquid-disordered (Ld) regions enriched in unsaturated glycerophospholipids. In native plasma membranes, Lo domains are generally thought to function as nanometer-sized, transient structures that constitute discrete signaling sites in the membrane (Garcia-Parajo *et al.*, 2014).

Lo membrane microdomains influence intra- and intercellular signaling by creating platforms for the oligomerization of cell surface receptors and recruitment of downstream effectors (Zuidscherwoude *et al.*, 2014). Lo membranes are enriched at cell–cell junctions (Resnik *et al.*, 2011; Kurrle *et al.*, 2013; Stahley *et al.*, 2014; Lewis *et al.*, 2019), axo-glial junctions (Honke *et al.*, 2002; Schafer *et al.*, 2004), and immune synapses (Dupre *et al.*, 2002; Hiltbold *et al.*, 2003; Nika *et al.*, 2006). The myelin membranes that wrap axons are also highly enriched in cholesterol and sphingolipids, forming phase-separated membrane domains distinct from the rest of the cell membrane (Yurlova *et al.*, 2011). Lo membrane domain enrichment often corresponds to highly curved membranes, including at caveolae (Lamaze *et al.*, 2017), viral budding sites (Sengupta *et al.*, 2019), and filopodia (Scorticati *et al.*, 2011; Honda *et al.*, 2017), where they play instructive roles in membrane remodeling. The observation that axon-associated membranes of epidermal cells are strongly labeled by a PIP2 sensor before neurite ensheathment (Jiang *et al.*, 2019) raises the possibility that membrane microdomains of distinct lipid composition initiate skin cell–neuron interactions. Given the roles of epidermal cells in modulating sensory neuron branching and function, membrane microdomains could be platforms that organize skin cell–neuron interactions during neurite branching in the skin and in mature skin at sites of functional skin cell–neuron coupling.

To study how sensory axons influence epithelial development, we imaged early stages of epidermal innervation in live zebrafish embryos. During embryonic stages, the peripheral axons of zebrafish somatosensory neurons initially grow and branch between the two epithelial layers of the epidermis: the outer periderm and inner basal layers (O'Brien *et al.*, 2012). Although axons make direct contact with both periderm and basal keratinocytes, as development proceeds they become ensheathed exclusively by the apical membranes of basal cells, and never by periderm cells (O'Brien *et al.*, 2012). Previous work identified the accumulation of a PIP2 biosensor underneath neurites as the earliest known step in neurite ensheathment, promoting the recruitment of downstream ensheathment channel components (Jiang *et al.*, 2019). However, it was unknown whether axon-associated membrane domains constitute a unique lipid environment.

Here we use quantitative imaging approaches to characterize the maturation of the lipid environment at axon-associated membrane domains, from the earliest stages of ensheathment to autotypic junction formation. We found that PIP2-containing membrane microdomains are indeed quantitatively enriched in PIP2 and multiple markers for Lo membrane, thus constituting distinct lipid microdomains. PIP2 microdomains are sites of F-actin–based protrusion and preferential cadherin enrichment well before autotypic junction formation. These cadherin-rich protrusions appear to mediate keratinocyte layer–specific interactions with axons. Consistent with this idea, live imaging of the initiation of ensheathment revealed that axons rapidly remodel initially isolated lipid microdomains into coherent axon-associated domains. In the absence of axons, these cadherin-enriched lipid microdomains formed excessive heterotypic junctions between periderm and basal cells, likely altering the adhesive properties of the epidermis. These findings demonstrate that sensory axons have the potential to dramatically influence basic epithelial cell properties.

RESULTS

Axon outgrowth organizes PIP2-containing membrane microdomains on basal keratinocytes

In zebrafish embryos, somatosensory axons initially grow and branch exclusively between the periderm and basal cell layers of the epidermis during the first day of development and become progressively ensheathed by basal cells over the next several days (O'Brien *et al.*, 2012). To determine how axon outgrowth affects the membranes of periderm and basal epithelial cells, we used confocal live imaging to follow keratinocyte membrane dynamics from 24–33 h post-fertilization (hpf) (1 d post-fertilization, dpf), a period of active axon branching in the epidermis and before the formation of axon sheaths (Jiang *et al.*, 2019). To label basal cell membranes, we expressed a EGFP-PLCδ-PH reporter for the phosphoinositide PIP2 under the control of an upstream activating sequence (UAS:EGFP-PLCδ-PH) using a *tp63*:GAL4VP16 BAC driver line (Rasmussen *et al.*, 2015). Axons

were labeled using either a pan-neuronal *neural beta tubulin:DsRed* transgene (Peri and Nüsslein-Volhard, 2008) or a somatosensory neuron-specific *isl1:Gal4;UAS:DsRed* line (Sagasti *et al.*, 2005).

As reported previously, EGFP-PLCδ-PH in basal cells initially concentrated in discrete microdomains at the apical membrane (Figure 1A; Supplemental Movie 1). As axons grew over basal cells, EGFP-PLCδ-PH microdomains became more prominent and accumulated underneath axons (Figure 1, A–A‴; Supplemental Movie 1). Microdomains accumulated immediately upon axon contact, under extending growth cones (Figure 1, A–A‴, cyan arrowheads; Supplemental Movie 1), as well as under axon shafts that had previously grown over basal cells (Figure 1, A–A‴, red arrows; Supplemental Movie 1). These microdomains were highly dynamic and reversibly associated with growing axons (Supplemental Movie 1).

By contrast, axons had dramatically fewer, and qualitatively distinct, effects on periderm membranes labeled with the same reporter. In many periderm cells, membranes were not appreciably affected by axon contact at 1 dpf (Figure 1, B–B‴, cyan arrowheads; Supplemental Movie 2). In others, outgrowing axons associated with scattered microdomains, but these microdomains did not coalesce into larger axon-associated membrane domains during the imaging interval (Supplemental Figure S1A, red arrows; Supplemental Movie 2). To characterize the consequences of periderm membrane–axon interactions, we imaged periderm cells expressing EGFP-PLCδ-PH and axons at 4 dpf, a stage when many axons are ensheathed by underlying basal cells (O'Brien *et al.*, 2012). We observed two distinct patterns in these cells: either EGFP-PLCδ-PH showed no distinct organization near axons or it appeared as discrete puncta ordered along axons (Supplemental Figure S1B, red arrows). Importantly, while EGFP-PLCδ-PH membrane microdomains in the basal layer underwent remodeling over time to form long, continuous ensheathment channels, the small EGFP-PLCδ-PH membrane microdomains in the periderm layer underwent no reorganization to form larger membrane domains (Supplemental Figure S1C). Thus, although axons dramatically remodel PIP2-containing microdomains in basal cells, in periderm cells, if such domains form at all, they remain small and discontinuous, indicating that axons preferentially associate with basal cells. Because only basal cells wrap axons into ensheathment channels, early membrane dynamics in basal cells may precede the formation of ensheathment channels (Jiang *et al.*, 2019).

Basal cell microdomains have a distinct lipid composition

Axon-associated microdomains in neurite-ensheathing epithelial cells in both flies and fish are enriched in EGFP-PLCδ-PH (Jiang *et al.*, 2019). These regions of increased fluorescence could be quantitatively enriched in the PIP2 lipid or simply contain greater membrane density. To distinguish between these possibilities, we generated a dual reporter that expressed the EGFP-PLCδ-PH sensor bicistronically with mRubyCAAX, a potentially "generic" prenylated membrane reporter, using a self-cleaving T2A peptide (Kim *et al.*, 2011). This dual membrane reporter was placed under UAS control (UAS:EGFP-PLCδ-PH-T2A-mRubyCAAX) and injected into *tp63:GAL4VP16* transgenic animals to mosaically label basal cells. Embryos were imaged by confocal microscopy at 1 dpf, when microdomains begin accumulating underneath axons. To estimate the levels of each reporter recruited into microdomains, we measured the ratio of each reporter inside versus outside microdomains (Figure 2A; see *Materials and Methods*), providing a measure of relative reporter enrichment. EGFP-PLCδ-PH and mRubyCAAX both labeled membrane microdomains in basal keratinocytes (Figure 2B, cyan arrowheads) and had relative enrichment values >1 (Figure 2B), indicating that membrane microdomains are most likely regions of increased membrane area. However, EGFP-PLCδ-PH was consistently more enriched in these domains than mRubyCAAX (Figure 2C). Thus, membrane microdomains strongly labeled by EGFP-PLCδ-PH are indeed enriched in PIP2, defining areas of distinct lipid composition in the apical membrane of basal keratinocytes.

Axon-associated PIP2 microdomains form both by reorganizing existing domains and by expanding domains at basal cell borders

PIP2 lipid microdomains could accumulate underneath axons either through the lateral coalescence of preformed microdomains or form de novo underneath axons. To determine how axons accumulate lipid microdomains in the underlying basal cell membrane, we made high-temporal-resolution (~20–30 s interval) time-lapse movies using a Fast Airyscan microscope (see *Materials and Methods*). This allowed us to unambiguously follow microdomains over time as they matured into elongated axon-associated membrane domains (Figure 3, A–C⁗; Supplemental Movie 3).

Frequently, we found that axon-associated membrane domains formed via lateral coalescence in which preformed microdomains converged toward axons, joining together before accumulating under the axon shaft (Figure 3D, left, cyan arrowheads; Supplemental Movie 3). By overlaying sequential frames of PIP2 lipid microdomains, we confirmed the lateral movement of lipid microdomains toward axons (Supplemental Figure S2, A–C). We also found evidence that microdomains sometimes form through the expansion of PIP2-rich membrane domains from the PIP2-enriched cell borders of basal cells (Figure 3D, right, cyan arrowhead; Supplemental Movie 3), suggesting that the PIP2-rich cell borders are sites of active lipid microdomain generation.

If axons indeed promote the lateral coalescence of lipid microdomains on the basal cell surface, microdomains should remain scattered in the absence of cutaneous axons. To test this prediction, we made time-lapse movies of basal cells in *neurogenin-1* (*ngn1)* morphants that entirely lack somatosensory skin innervation (Andermann *et al.*, 2002; O'Brien *et al.*, 2012). In *ngn1* morphants, basal cells formed PIP2 lipid microdomains, but these domains did not coalesce into extended structures over the course of 3 h at 1 dpf (Supplemental Figure S2D; Supplemental Movie 4). Thus, axons are not required for microdomain formation, but rather to direct their reorganization.

A potential mechanism of microdomain formation was suggested while capturing basal cell division events during axon outgrowth (Supplemental Movie 5). Rounding mitotic basal cells (asterisk in Supplemental Movie 5) pulled on nearby nondividing basal cells; PIP2 microdomains rapidly disassembled as the nondividing cell was pulled toward the dividing cell. As the nondividing cell relaxed, microdomains formed rapidly and specifically around axon shafts (Supplemental Movie 5). This observation suggests that microdomain formation could involve a local reduction in membrane tension as an axon presses against the basal cell membrane. De novo formation could, therefore, reflect a passive remodeling of the basal cell surface as axons crawl over them (e.g., depression). However, lipid microdomain accumulation is restricted to some axonal segments, while others induce no remodeling of the basal cell surface (Supplemental Figure S2, E–E⁗; Supplemental Movie 6), suggesting that microdomain accumulation is a consequence of specific recognition of axons. In a previous study we found that, similarly, ~60% of sensory axon branches are selectively ensheathed by basal cells (Jiang *et al.*, 2019), raising the possibility that those

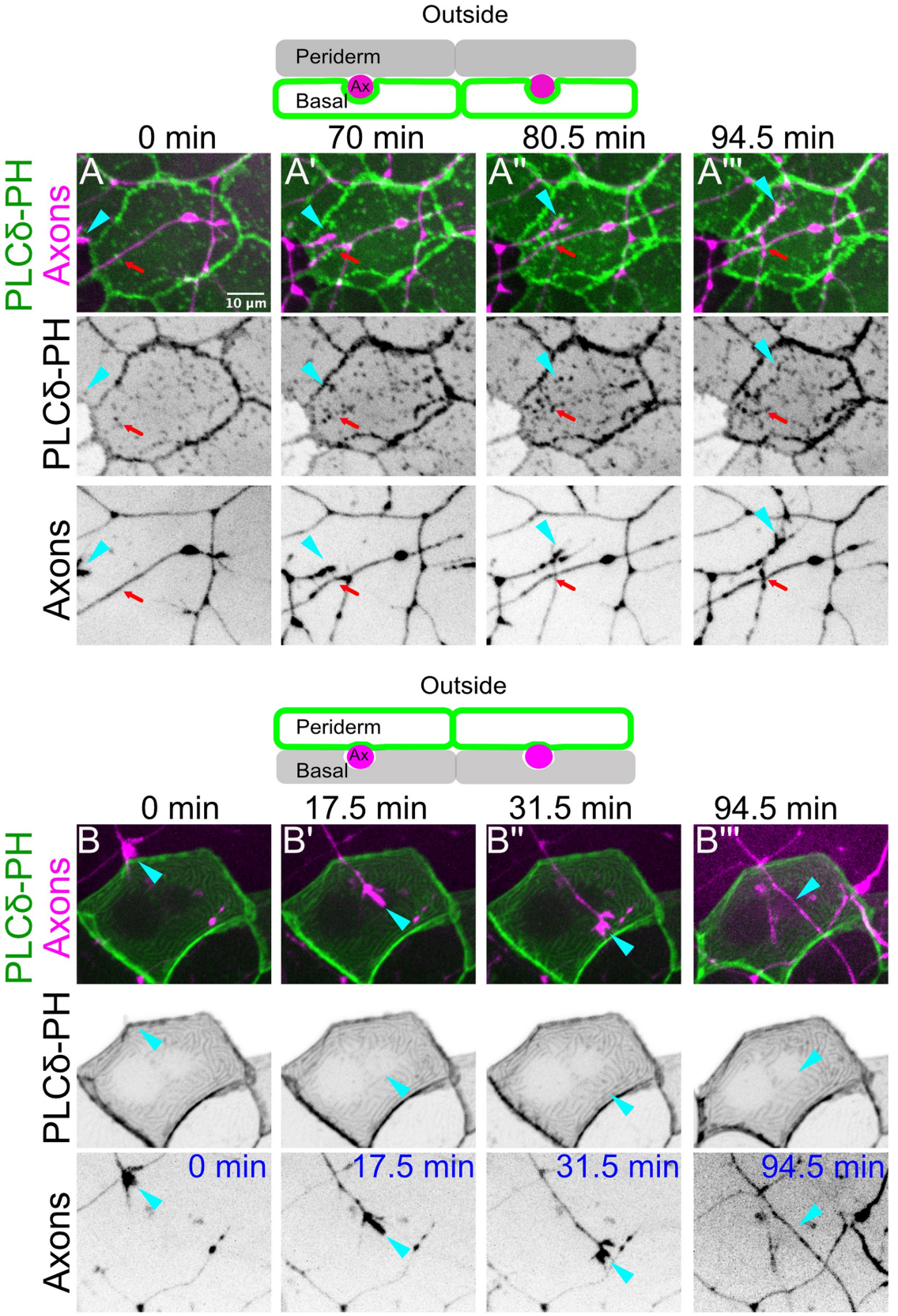

FIGURE 1: Somatosensory axons induce epidermal layer–specific membrane remodeling. (A) (Top) Schematic of reporter expression in panels A–A‴. The basal cell plasma membrane was labeled with a PIP2 reporter (Tg(*tp63*:GAL4VP16; UAS:EGFP-PLCδ-PH, green), and somatosensory neurons (magenta) were labeled with *neural beta tubulin::DsRed* or *isl1*:GAL4VP16; UAS:DsRed transgenes. (A–A‴) Stills from a time-lapse movie. An extending neurite (cyan arrowhead) grew over the apical-facing surface of a basal cell. Shortly after the appearance of the

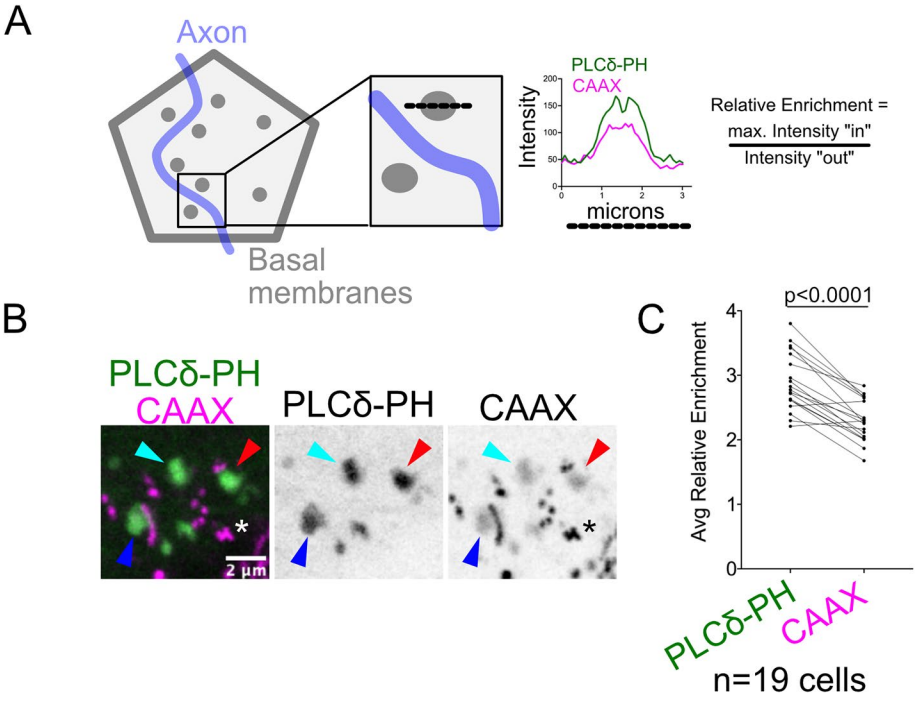

FIGURE 2: Basal cell membrane microdomains are enriched in a PIP2 reporter. (A) (Left) Schematic showing how relative reporter enrichment was quantified. Lipid microdomains are represented in gray, axon (not imaged) in blue. Intensity plots for EGFP-PLCδ-PH and mRubyCAAX were generated along a line drawn across microdomains (dotted black line). (Right) Intensity plot from a representative microdomain. To calculate relative enrichment, the maximum intensity within the microdomain was divided by the intensity of each membrane reporter just outside the microdomain. (B) Image of basal cell membrane coexpressing EGFP-PLCδ-PH and mRubyCAAX at 1 dpf. Microdomains were labeled by both reporters (arrowheads), but GFP was more enriched. mRubyCAAX also accumulated in numerous aggregates and/or endosomes in basal cells (asterisk). (C) Quantification of relative enrichment of the two membrane reporters in isolated microdomains (204 microdomains measured from 19 cells from seven embryos). Enrichment values from the same basal cell clones were averaged to obtain the average relative enrichment for each cell. EGFP-PLCδ-PH was significantly more enriched in microdomains than mRubyCAAX ($p < 0.0001$, paired *t* test).

axons that induce microdomain accumulation may be destined to be ensheathed.

The high temporal resolution of our live imaging allowed us to classify lipid microdomains based on their behavior over the course of 30 min time-lapse imaging (Figure 3E). The majority of lipid microdomains (78.9%) persisted through the entire imaging interval: of these, 43.6% persisted as isolated microdomains, 25.7% underwent fusion to form larger domains, and 9.6% split to form multiple, smaller microdomains. Only 21.2% of lipid microdomains disappeared during the 30 min imaging interval. Thus, lipid microdomains are stable structures that undergo remodeling, with a bias toward fusing to form larger domains. Microdomain fusion likely reflects their coalescence to form axon-associated membrane domains.

Lipid microdomains are sites of F-actin–based protrusion

PIP2 can regulate the cortical actin cytoskeleton by recruiting several actin-binding proteins (Janmey *et al.*, 2018). To determine whether F-actin associates with basal cell PIP2 microdomains, we imaged the actin reporter LifeAct-mRuby. To covisualize lipid microdomains and the actin cytoskeleton, the UAS:LifeAct-mRuby plasmid was injected into *tp63*:GAL4VP16;UAS:EGFP-PLCδ-PH embryos, and the embryos were imaged at 1 dpf by time-lapse confocal microscopy. Isolated PIP2 lipid microdomains were enriched in LifeAct signal (Figure 4A; Supplemental Movie 7), demonstrating that lipid microdomains define sites of preferential F-actin polymerization and/or stabilization. However, F-actin was not recruited uniformly at lipid microdomains, but rather was concentrated within subregions (Figure 4A, bottom intensity plots), suggesting that lipid microdomains are compartmentalized. LifeAct-mRuby fluorescence at lipid microdomains fluctuated and sometimes receded while the PIP2 microdomain remained stable (Figure 4A, bottom intensity plots). Thus, PIP2 lipid microdomains are sites of dynamic F-actin remodeling, but PIP2 enrichment alone is not sufficient for F-actin stabilization. We propose that PIP2 lipid microdomains may reversibly recruit factors that promote the stability of F-actin at microdomains.

The accumulation of F-actin at microdomains suggests that these domains could form protrusions that associate with axons. To visualize cortical F-actin with high spatial and temporal resolution, we used a Fast Airyscan microscope to make time-lapse movies of cutaneous axons growing over basal cells expressing LifeAct-GFP (*tp63*:GAL4VP16;UAS:LifeAct-GFP) (Rasmussen *et al.*, 2015). We found that protrusive F-actin structures dynamically wrapped around axon shafts (Figure 4, B and C, cyan arrowheads; Supplemental Movie 8). EGFP-PLCδ-PH fluorescence appeared concomitantly with the appearance of F-actin (Supplemental Movie 7), suggesting an association between PIP2 production and F-actin polymerization at the apical surface of basal cells. As with EGFP-PLCδ-PH, F-actin association with axons was selective, with some axon branches eliciting numerous F-actin protrusions (Supplemental Movie 6, cyan arrowhead), whereas others were ignored by basal cells (Supplemental Movie 6, red arrowhead). We conclude that PIP2 lipid microdomains are sites of dynamic F-actin polymerization/stabilization, resulting in the formation of membrane protrusions

axon, EGFP-PLCδ-PH–labeled membrane microdomains accumulated underneath the axon. Red arrow shows scattered microdomains that accumulated under an axon that had already grown over the basal cell. See Supplemental Movie 1. (B) (Top) Schematic of reporter expression in panels B–B‴. Periderm cell plasma membranes (green) were mosaically labeled with a UAS:EGFP-PLCδ-PH transgene injected into Tg(*krt5*:GAL4FF); Tg(*neural beta-tubulin*:DsRed) embryos. Axons are labeled in magenta. (B–B‴) Stills from a time-lapse movie. Axons had no apparent effect on the plasma membrane of overlying periderm cells. Cyan arrowhead marks a growth cone crawling underneath the labeled periderm cell in B–B″ and the axon shaft after the growth cone has passed in B‴. See Supplemental Movie 2.

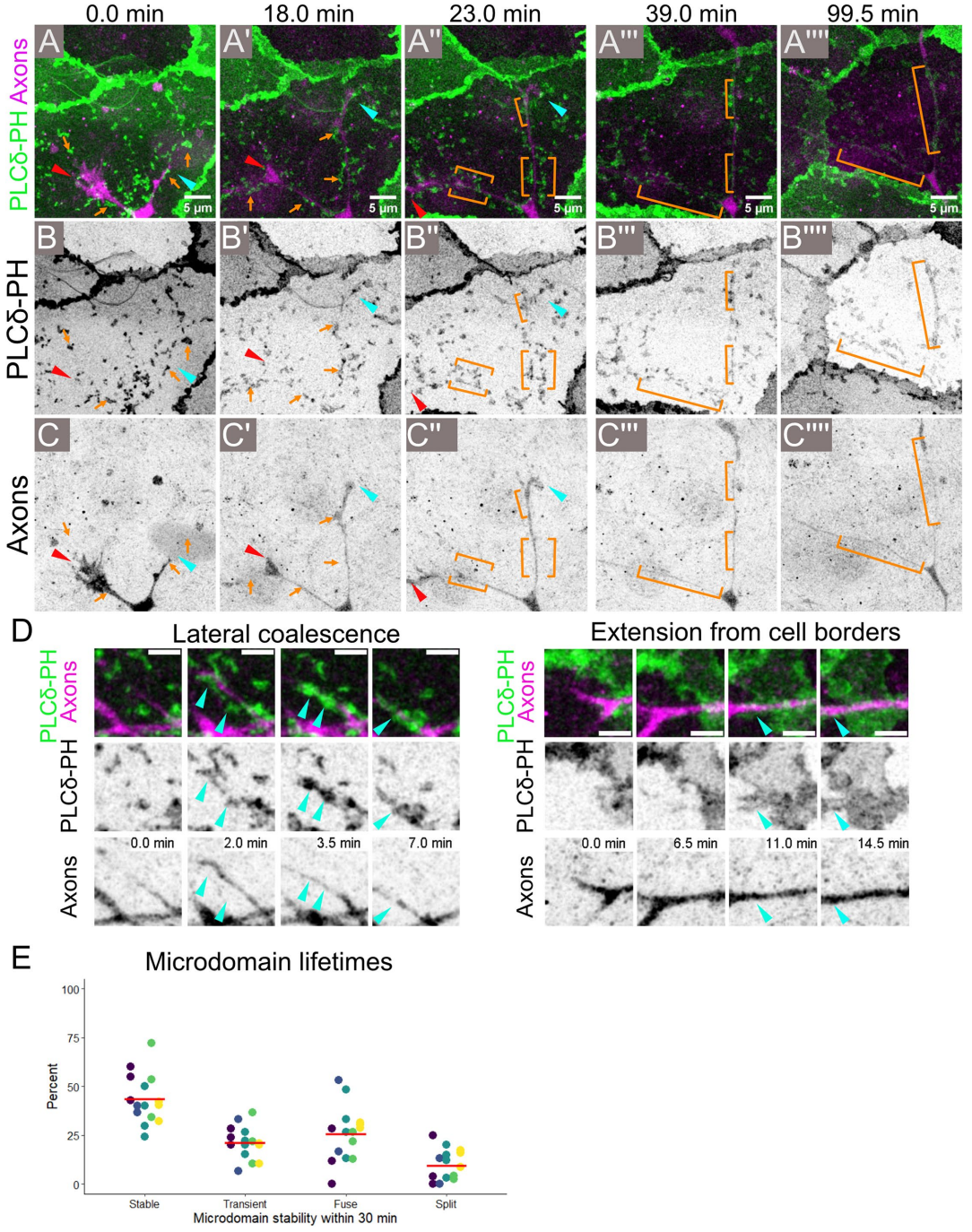

FIGURE 3: Axons reorganize epithelial PIP2 microdomains by lateral coalescence or extension from cell borders. (A–C′′′′) Stills from a Fast Airyscan movie of a 1 dpf Tg(*tp63*:GAL4VP16; UAS:EGFP-PLCδ-PH); Tg(*neural beta tubulin*:DsRed) embryo. Sensory axons are labeled in magenta and EGFP-PLCδ-PH in green. As growth cones (red and cyan arrowheads) from an axon first grow over a basal keratinocyte, the apical surface of the keratinocyte contains scattered PIP2 lipid microdomains (orange arrows). By 18–23 min, a subset of lipid microdomains have accumulated in the proximity of axons (orange brackets in A′′–C′′ and A′′′–C′′′). By 99.5 min, lipid microdomains have formed elongated axon-associated membrane domains (orange brackets in A′′′′–C′′′′). Images were acquired every 30 s. See Supplemental Movie 3. (D) Stills from Fast Airyscan movies of 1 dpf Tg(*tp63*:GAL4VP16; *UAS*:EGFP-PLCδ-PH); Tg(*neural beta tubulin*:DsRed) embryos showing different modes of lipid microdomain association with axons (arrowheads). (Left) Preexisting lipid microdomains coalesced underneath an axon segment. See Supplemental Movie 3. (Right) In other cases, an axon passing over a basal cell boundary was followed by PIP2-rich membrane from the cell borders. Images were acquired every 30 s. See Supplemental Movie 3. (E) Classification of microdomains into categories based on their behavior in 30 min movies (20 s imaging intervals). A total of 43.6% of microdomains were stable, persisting as isolated domains through the entire imaging interval; 25.7% of microdomains fused with other microdomains, while 9.6% formed by splitting from existing microdomains; 21.2% of microdomains were transient structures that disappeared during the course of the live imaging. Data from 15 cells (dots) from five embryos (color coded).

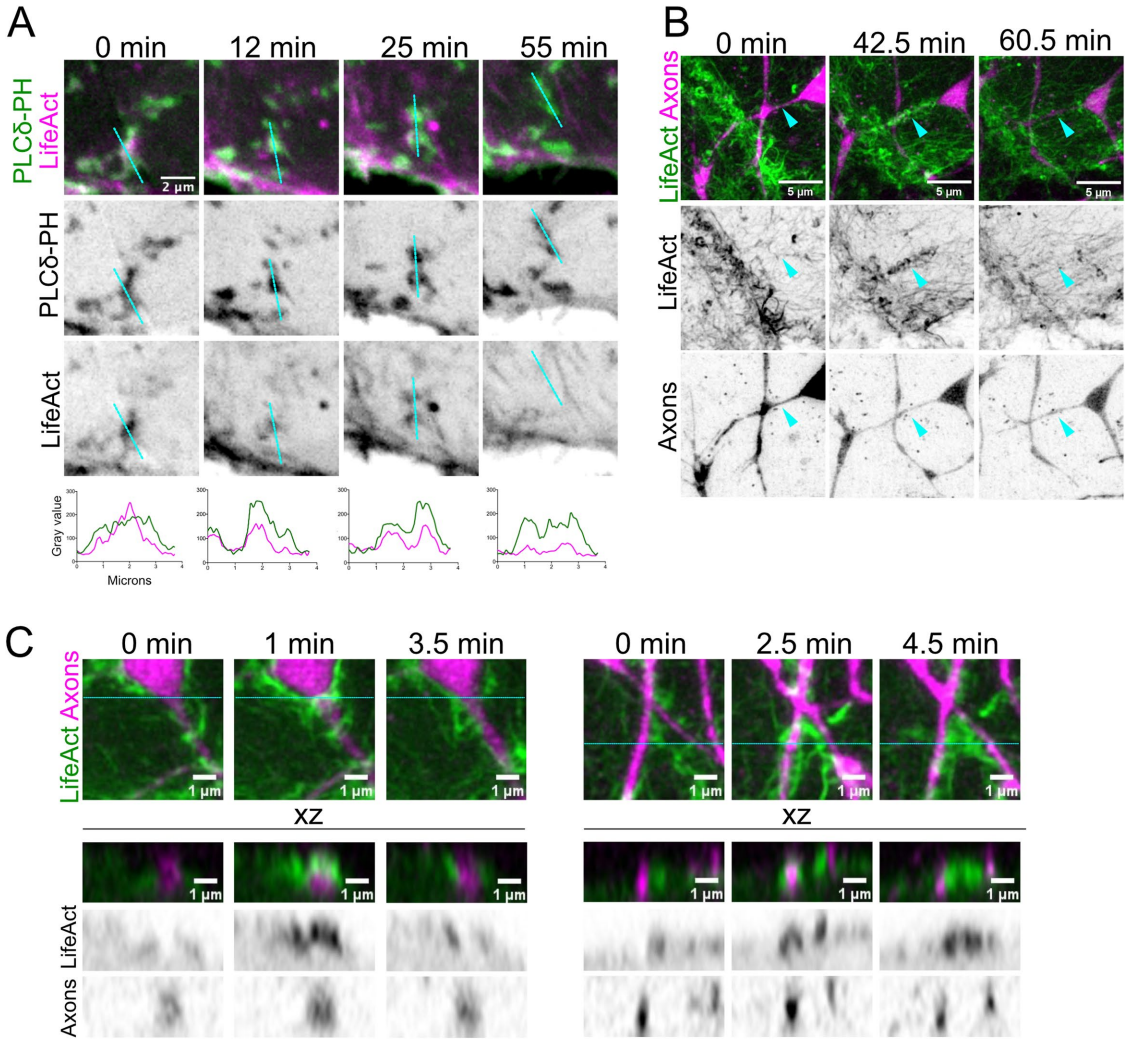

FIGURE 4: Basal cells form F-actin protrusions around axons. (A) (Top) Stills from movies of 1 dpf Tg(*tp63:GAL4VP16;*UAS:EGFP-PLCδ-PH) injected with a 10xUAS:LifeAct-mRuby plasmid. The F-actin reporter signal (magenta) reorganized concomitantly with microdomain (green) remodeling. See Supplemental Movie 7. (Bottom) Linear intensity plots through the indicated cyan lines above showing the dynamic recruitment of F-actin to lipid microdomains. (B) Stills from a 1 dpf Tg(*tp63:GAL4VP16;*UAS:LifeAct-GFP);Tg(*neural beta tubulin:DsRed*) embryo taken by Fast Airyscan. During the initial outgrowth of sensory axons (magenta) into the skin, F-actin (green) recruited underneath axons dynamically wrapped axon segments (cyan arrowheads). See Supplemental Movie 8. Images were acquired every 30 s. (C) Two representative orthogonal stills from movies of the axon–basal keratinocyte interface from 1 dpf Tg(*tp63:GAL4VP16;*UAS:LifeAct-GFP);Tg(*neural beta tubulin:DsRed*) embryos imaged by Fast Airyscan (30 s intervals). Cyan lines in en face images indicate positions of orthogonal optical slices (bottom, "xz" panels). F-actin filaments (green) are recruited to the apical-facing cortex underlying axons (magenta) and surround the axon shaft (left, "1 min" still; right, "2.5" min still). Images were acquired every 30 s.

that reversibly wrap axons. F-actin production may allow protrusions to extend and retract dynamically during this process to sample the axonal surface and distinguish axons that will be ensheathed from those that will not.

Axon-associated microdomains become progressively enriched in liquid-ordered membrane reporters

Because membrane microdomains have a distinct lipid composition, we asked whether axon-associated membranes had other distinct lipid properties. Lipid rafts are membrane nanodomains enriched in cholesterol and sphingolipids; the bulky hydrophobic moieties in these lipids promote the formation of nanometer-sized Lo membrane phases (Figure 5A), which can coalesce into microdomains that serve as platforms for cell–cell interactions (Zuidscherwoude *et al.*, 2014). To determine whether axon-associated microdomains are enriched in Lo membranes, we generated dual membrane reporters based on previously validated reporters that quantitatively partition into Lo and Ld (raft vs. nonraft) membranes (Figure 5A) (Pyenta *et al.*, 2001; Zacharias *et al.*, 2002; Sengupta *et al.*, 2019). We used the double myristoylated ("m") and palmitoylated ("p") lipid modifications (mp-mEGFP and mp-mApple) and a GPI-anchored SuperFolder GFP (sfGFP-GPI) as Lo reporters and adapted geranylgeranylated fluorescent reporters (mEGFP-gg and mApple-gg) as Ld reporters. Because intrinsic fluorescent protein properties can promote Lo membrane–independent clustering (Zacharias *et al.*, 2002), we used a variant of EGFP mutated to prevent oligomerization (mp-EGFP A206K, L221K, F223K, hereafter called mp-mEGFP; see *Materials and*

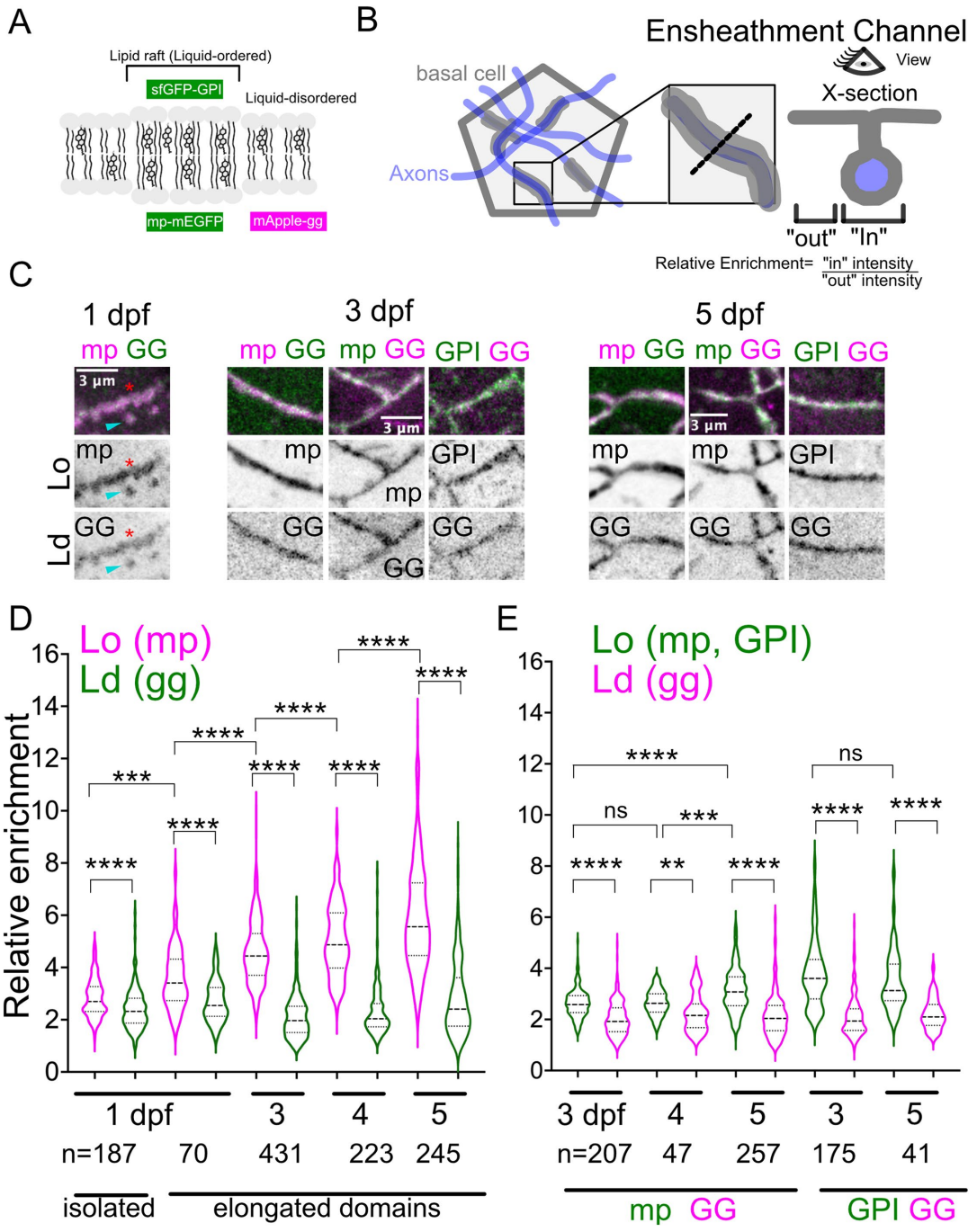

FIGURE 5: Axon-associated domains progressively enrich reporters for Lo, but not Ld, membrane. (A) Double myristoylation and palmitoylation, or modification by glycosylphosphatidylinositiol anchors, localizes fluorescent protein reporters preferentially in Lo membrane. Gernanylgeranylated fluorescent reporters were used to label Ld membrane. (B) Schematic of membrane reporter localization (gray) with respect to axons (blue). Inset shows detail of axon-associated membrane domain (AAD). Relative enrichment of each membrane reporter was measured using the ratio of each reporter inside ("In") to outside ("Out") AADs. (C) Details of AADs in basal cells expressing Lo and Ld reporters bicistronically. Lo and Ld reporters were imaged between 1 and 5 dpf. At 1 dpf, relative enrichment was measured in both isolated microdomains (yellow arrowheads, "isolated" in D) and larger axon-associated domains (red asterisks, "elongated domains" in D) (D) Relative enrichment of AADs from basal cells expressing mp-mApple-T2A-mEGFP-gg. mp-mApple (Lo reporter) exhibited significantly greater relative enrichment than mEGFPgg (Ld reporter) at 1, 3, 4, and 5 dpf (**** $p < 0.0001$, Wilcoxon signed rank tests). Over time, the relative enrichment of mp-mApple increased significantly (*** $p < 0.001$, ANOVA with paired *t* test; **** $p < 0.0001$, ANOVA with Mann–Whitney U test). (E) Relative enrichment of AADs from basal cells expressing mp-mEGFP-T2A-mApple-gg or sfGFP-GPI-T2A-mApple-gg at 3, 4, and 5 dpf. Greater relative Lo enrichment was independent of fluorescent protein combination and can be recapitulated using an independent Lo reporter (sfGFP-GPI) (** $p < 0.01$, **** $p < 0.0001$, Wilcoxon signed rank tests). mp-mEGFP shows significantly greater enrichment at 5 dpf vs. 4 dpf (*** $p < 0.001$, ANOVA with Mann-Whitney U test) and vs. 3 dpf (**** $p < 0.0001$, ANOVA with Mann–Whitney U test).

Methods). We coexpressed Lo and Ld reporters in the same basal cells using a T2A peptide to measure the relative enrichment of each reporter within ("In") and outside ("Out") axon-associated membranes (Figure 5B).

At 1 dpf, lipid microdomains were found as either isolated structures or elongated membrane domains (presumably axon associated). Isolated microdomains at 1 dpf were more enriched in the Lo reporter mp-mApple than the Ld reporter mEGFP-gg (Figure 5, C, cyan arrowhead, and D; $p = 7.21e\text{-}11$, Wilcoxon signed rank test). Relative enrichment of the Lo reporter increased following the formation of elongated membrane domains, with increasing Lo enrichment observed as axon-associated membrane domains matured into ensheathment channels by 4–5 dpf (Figure 5D; 1 dpf: $p = 8.31e\text{-}7$; 3–5 dpf: $p < 2.2e\text{-}16$; Wilcoxon signed rank tests; Supplemental Figure S3A). To rule out fluorescent protein–specific effects, we swapped the fluorophores between the dual Lo/Ld reporters (mp-EGFP-T2A-mApple-gg). As with mp-mApple, mp-mEGFP was more enriched than the Ld reporter between 3 and 5 dpf (Figure 5E; 3 dpf: $p < 2.2e\text{-}16$; 4 dpf: $p = 0.002$; 5 dpf: $p < 2.2e\text{-}16$; Wilcoxon signed rank tests; Supplemental Figure S3B). To rule out the possibility that the putative Lo enrichment was an artifact of the myristoylation and palmitoylation modifications, we used the sfGFP-GPI reporter for Lo membranes. Similar to mp-mApple and mp-mEGFP, sfGFP-GPI was significantly more enriched at axon-associated domains than mApple-gg (Figure 5E; 3 dpf: $p < 2.2e\text{-}16$; 5 dpf: $p = 6.23e\text{-}11$; Wilcoxon signed rank tests; Supplemental Figure S3C). Lower relative enrichment of Ld reporters (mApple-gg and mEGFP-gg) was at least partly due to increased cytosolic signal compared with the Lo reporters, which showed more stable membrane recruitment, confirming that the different lipid modifications used in these reporters are distinctly regulated. We also found that EGFP-PLCδ-PH exhibited greater relative enrichment at axon-associated membranes compared with mApple-gg (Supplemental Figure S3, D and E), suggesting that PIP2 may also be enriched within the Lo membranes around axons. Collectively, these results indicate that distinct lipid-modified proteins show specific preferences for axon-associated membranes, raising the possibility that lipid raft–enriched membranes accumulate preferentially around axons.

Myristoylated and palmitoylated Lo reporters were increasingly enriched at axon-associated membrane domains from 1–5 dpf, whereas relative enrichment of the Ld reporter remained relatively constant (Figure 5, D and E; see Supplemental Table 1 for statistics). This observation suggests that axon-associated membranes mature over time by changing their lipid composition. The GPI-anchored Lo reporter showed the greatest relative enrichment regardless of stage, indicating that sfGFP-GPI recruitment reaches its maximum earlier than the mp Lo reporter. Collectively, these results suggest that lipid microdomain association with axons promotes the accumulation of Lo membranes at sites of future ensheathment channels and could facilitate ensheathment channel formation by clustering proteins and/or promoting membrane curvature (Sengupta *et al.*, 2019).

Lipid microdomains accumulate junction proteins that contribute to ensheathment channel formation

The final step of sensory neurite ensheathment is the recruitment of junctions to epithelial membranes surrounding neurites (Jiang *et al.*, 2019). Because junction-forming proteins can partition preferentially into Lo membranes (Lewis *et al.*, 2019), we hypothesized that lipid microdomains in basal cells enrich cadherins that will later form autotypic junctions at ensheathment channels. To test this idea, we expressed fluorescently tagged adherens junction and desmosomal cadherins, which are both found at ensheathment channels (Jiang *et al.*, 2019). To visualize E-cadherin (E-cad), we used a *cdh1-TdTomato* gene trap line reporting endogenous E-cad (Cronan *et al.*, 2018). To visualize Desmocollin 2–like (Dsc2l), we used a bacterial artificial chromosome (BAC) reporter expressing GFP-tagged Dsc2l under endogenous regulatory elements. Isolated PIP2 lipid microdomains in basal cells were enriched in E-cad (Figure 6, A–-B″, and E) and Dsc2l (Supplemental Figure S4, A–B″, and E) at 1 dpf, well before ensheathment channels form. Cadherin localization to microdomains was heterogeneous, often appearing to cluster within subregions of PIP2 microdomains (red arrows, Figure 6, D–D″), suggesting that their enrichment to microdomains was not simply a consequence of increased membrane in those areas. Interestingly, Dsc2l showed stronger relative enrichment than E-cad at microdomains (compare Figure 6E with Supplemental Figure S4E), suggesting that desmosomal and adherens junction cadherins may be recruited or stabilized at lipid microdomains by distinct mechanisms. Thus, microdomain accumulation at axon contact sites may promote the recruitment of junction proteins needed for subsequent ensheathment.

To test whether microdomain lipid composition promotes the recruitment of junction proteins, we treated fish acutely with methyl-β-cyclodextrin (MBCD), which disrupts Lo membranes by extracting cholesterol (Zidovetzki and Levitan, 2007). This treatment modestly reduced E-cad enrichment at ensheathment channels (Supplemental Figure S3F). While the effects of MBCD are not restricted to Lo membrane domains (Zidovetzki and Levitan, 2007), this result suggests that Lo membranes may be required for the maintenance of junction proteins at ensheathment channels.

Lipid microdomains enrich E-cadherin independently of axons

Basal cell cadherins may be recruited to ensheathment channels by axons directly, or by PIP2- and Lo-enriched microdomains that coalesce into axon-associated domains. To distinguish between these possibilities, we asked whether cutaneous axons are required for cadherin recruitment to microdomains, and whether lipid microdomains in basal cells mature independently of axons. To test the requirement for axons in cadherin recruitment to lipid microdomains, we compared endogenous E-cad recruitment in microdomains in 1 dpf control morphants, which had not yet coalesced into axon-associated domains, to its recruitment in microdomains in *ngn1* morphants. E-cad was enriched to similar extents in wild-type (WT) control and *ngn1* morphant microdomains at 1 dpf (Figure 6, A–F). To determine whether lipid microdomains continue to mature in the prolonged absence of axons, we measured E-cad enrichment in *ngn1* morphants at 4 dpf (Figure 6, I and J), when axons are normally sealed by autotypic junctions into ensheathment channels (Figure 6, G and H). Compared to "early" microdomains in 1 dpf control and *ngn1* morphants, "late" microdomains in both control and *ngn1* morphants were more enriched in E-cad (compare Figure 6, K and L, with Figure 6, E and F). On the other hand, the desmosomal cadherin Dsc2l was recruited early and strongly to lipid microdomains; Dsc2l enrichment was maintained over time, and in the absence of axons (Supplemental Figure S4). Thus, lipid microdomains function to recruit and enrich cadherins that will later seal axons in ensheathment channels. Cadherin enrichment occurs independently of axons, indicating that cadherin compartmentalization is an intrinsic function of these lipid microdomains.

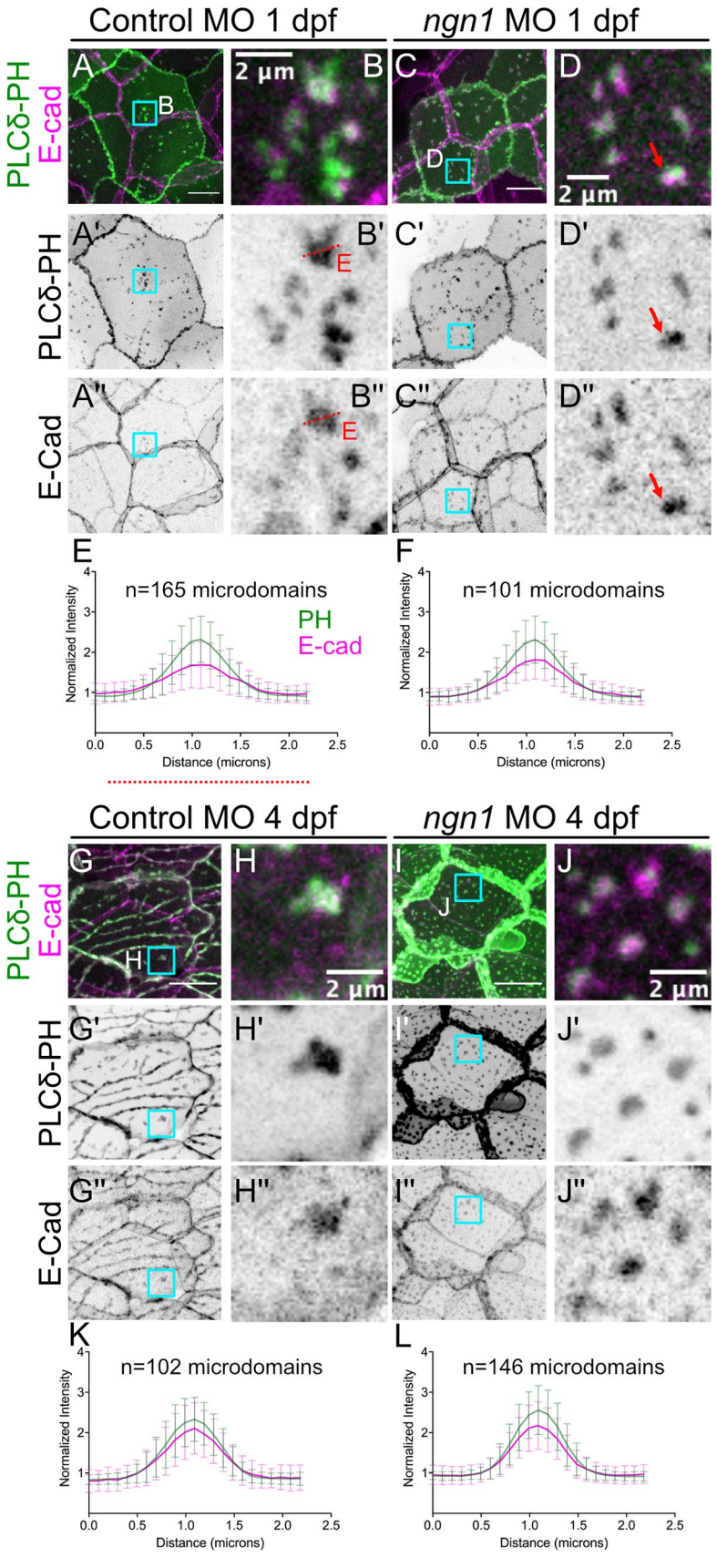

FIGURE 6: Lipid microdomains accumulate cadherins independently of axons. (A–B″) To measure E-cad recruitment to lipid microdomain before axon association, Tg(*tp63:GAL4VP16*; UAS:EGFP-PLCδ-PH); *cdh1*-TdTomato embryos were injected with a control morpholino (Ctrl MO; see *Materials and Methods*) and imaged at 1 dpf. (A–A″) Whole-cell view of a WT control basal cell with a PIP2 reporter (green) expressed specifically in basal cells and endogenous E-cad (magenta) expressed in both periderm and basal cells. The E-cad signal that does not overlap with the basal cell boundaries is from the overlying periderm layer. (B–B″) Detail of basal cell marked by inset (cyan box in A) showing recruitment of E-cad (B″) to PIP2 microdomains (B′) before their reorganization into ensheathment channels. (C–D″) To measure E-cad recruitment to early microdomains in the absence of axons, Tg(*tp63:GAL4VP16*; UAS:EGFP-PLCδ-PH); *cdh1*-TdTomato embryos were injected with a *neurogenin-1* morpholino (*ngn1* MO) and imaged at 1 dpf. (C–C″) Whole-cell view of *ngn1* morphant basal cells. (D–D″) Detail of PIP2 microdomains (D′) showing axon-independent recruitment of E-cad (D″). Red arrows show an example of heterogeneous E-cad enrichment within a lipid microdomain. (E, F) To compare E-cad recruitment in microdomains in the presence (E) or absence (F) of axons, E-Cadherin-TdTomato and EGFP-PLCδ-PH intensities were measured across linear ROIs spanning microdomains (red dotted lines in B′ and B″) and normalized to average fluorescence in the surrounding membrane. E-cad was weakly enriched in lipid microdomains before axon association (E), and this was unchanged by the absence of axons (F). (G–H″) Representative images of 4 dpf Tg(*tp63:GAL4VP16*; UAS:EGFP-PLCδ-PH); *cdh1*-TdTomato larvae injected with control MO. E-cad recruitment to isolated microdomains (H–H″, K) increased relative to 1 dpf (compare K with E). To measure E-cad recruitment in the prolonged absence of axons Tg(*tp63:GAL4VP16*; UAS:EGFP-PLCδ-PH); *cdh1*-TdTomato embryos were injected with a *neurogenin-1* morpholino (*ngn1* MO) and imaged at 4 dpf (I–J″, L). PIP2 microdomains that formed in the absence of axons were still able to recruit and enrich E-cad to levels similar to those of microdomains that formed in WT basal cells (compare L vs. K). (Scale bars in A, C, G, I, 10 µm.)

Axon-mediated recruitment of cadherin-enriched microdomains into ensheathment channels inhibits the formation of basal cell–periderm heterotypic junctions

What happens to lipid microdomains in the absence of axons? The observation that they continue to accumulate cadherins suggested that the absence of axons might cause increased heterotypic junctions to form between periderm and basal cells. This hypothesis predicts that, in the absence of axons, 1) the number of apical microdomains in basal cells should increase; 2) these domains should stabilize over time; 3) similar stable domains in periderm membranes should associate with apical microdomains in basal cells; and 4) increased basal–periderm junctions should be detectable ultrastructurally.

To test the first prediction, we compared the density of isolated PIP2+Ecad+ microdomains in control and *ngn1* morphants at 3 dpf (Figure 7, A–C, cyan arrowheads), a stage when axons are sealed by autotypic contacts into ensheathment channels in WT animals (red arrows in Figure 7A) (O'Brien *et al.*, 2012). In the control epidermis, PIP2+Ecad+ microdomains were observed primarily at axon ensheathment channels; isolated PIP2+Ecad+ microdomains formed in regions devoid of ensheathment channels (Figure 7A, cyan arrowheads). Consistent with this

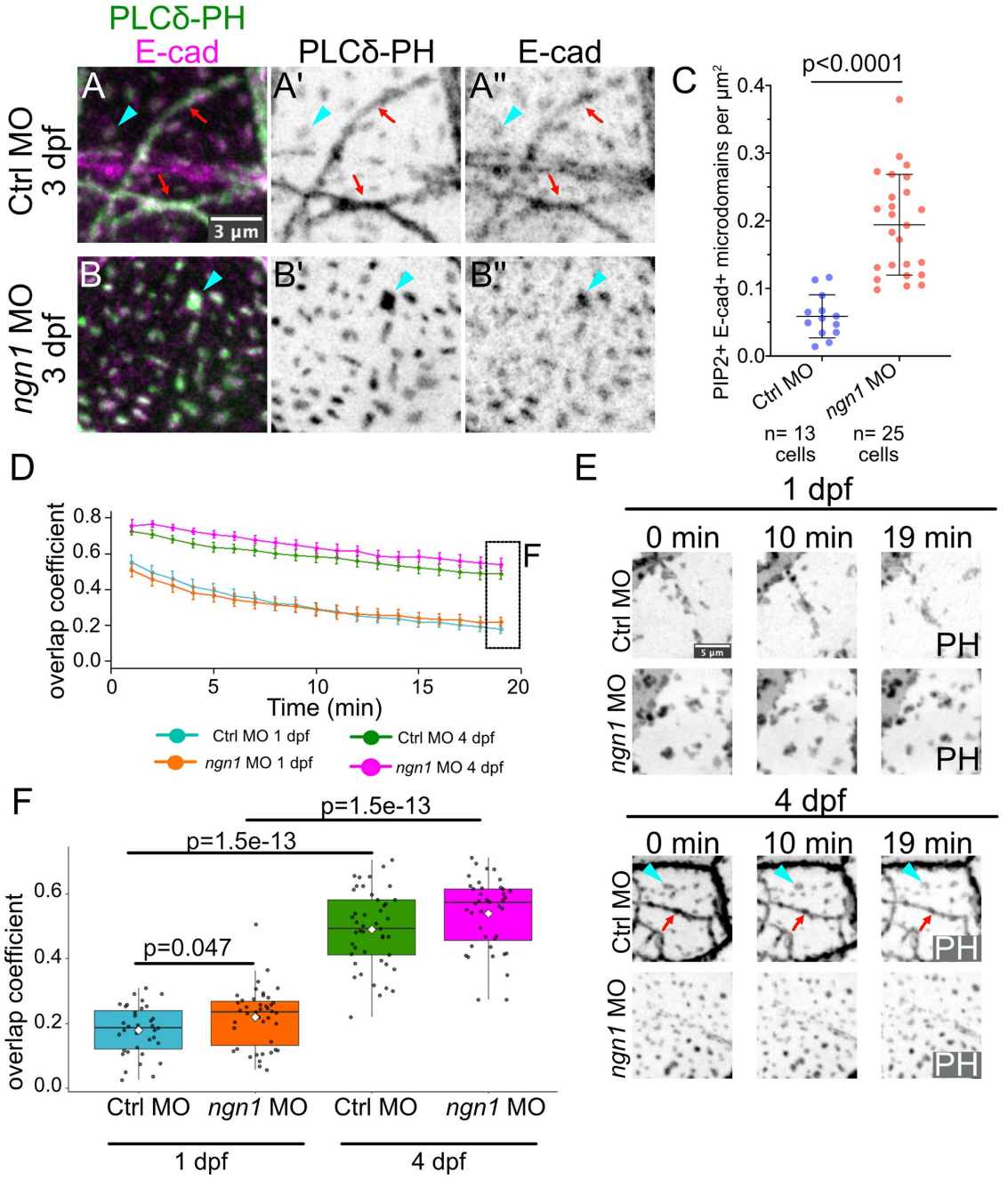

FIGURE 7: In the absence of axons, microdomains mature into stable periderm–basal contacts. (A) Tg(*tp63:*GAL4VP16;UAS:EGFP-PLCδ-PH); *cdh1*-TdTomato embryos injected with Ctrl MO or *ngn1* MO and imaged at 3 dpf. In WT controls (A–A″), E-cad in the basal layer localized to ensheathment channels (red arrows) and isolated microdomains (cyan arrowhead). In the absence of axons (B–B″, C), basal cells formed an increased number of E-cad–containing isolated microdomains (*p* value computed using Welch's *t* test, three embryos per condition). (D–F) One-minute-interval time-lapse movies of basal cell lipid microdomains were made using a conventional laser scanning confocal in Tg(tp63:GAL4VP16;*UAS:*EGFP-PLCδ-PH) embryos injected with control MO or *ngn1* MO. See Supplemental Movie 9. In D, the overlap coefficient of each frame to the first frame of the movie is plotted over time to measure the dynamics of lipid microdomains unassociated with axons in four conditions. The data points (overlap coefficient = 1.0) of the first frame to the first frame is omitted in each condition. (E) Stills from representative movies are shown. Cyan arrowhead shows an example of a microdomain unassociated with ensheathment channels (red arrows). At 1 dpf, isolated lipid microdomains were highly dynamic structures, while at 4 dpf they were static structures, resulting in higher overlap coefficients. See Supplemental Movie 9. (F) Comparison of endpoint overlap coefficients for individual basal cells for each condition (*p* values computed using Mann–Whitney U tests. Ctrl MO 1 dpf, $n = 35$ basal cells from five embryos; *ngn1* MO 1 dpf, $n = 43$ cells from four embryos; control MO 4 dpf, $n = 45$ cells from four embryos; *ngn1* MO 4 dpf, $n = 40$ cells from four embryos).

prediction, in the absence of axons, the number of isolated PIP2+Ecad+ microdomains on basal cell membranes dramatically increased (Figure 7, B and C).

To test the second prediction—that microdomains should stabilize over time—we analyzed microdomain dynamics at the apical membrane of basal cells in the presence and absence of axons in Tg(*tp63*:GAL4VP16;UAS:EGFP-PLCδ-PH) embryos (Figure 7, D–F). To quantify microdomain dynamics, we made 1-min-interval movies of EGFP-PLCδ-PH–labeled lipid microdomains and measured the overlap coefficient of each frame to the first frame. At 1 dpf, microdomains in *ngn1* morphants showed dynamics comparable to those of isolated microdomains in control morphants at the same stage (Figure 7, D, cyan and orange lines, and F; Supplemental Movie 9). However, in 4 dpf *ngn1* morphants, membrane microdomains became markedly static structures, showing significantly higher overlap coefficients than microdomains from 1 dpf *ngn1* morphants (Figure 7, D and F; Supplemental Movie 9). The dynamics of these ectopic lipid microdomains in 4 dpf *ngn1* morphants closely matched those of relatively sparse microdomains not associated with ensheathment channels in WT controls at the same stage (Figure 7, D and F; Supplemental Movie 9), indicating that the formation of stable microdomains is not an artifact of the complete loss of axons in the skin. We conclude that, over time, lipid microdomains not associated with axons reduce their lateral motion and become static membrane domains.

Though lipid microdomains mature independently of axons, axons modestly promoted microdomain dynamics in 1 dpf embryos (Figure 7F). While imaging lipid microdomains in 1 dpf WT embryos, we observed instances of transient lipid microdomain ordering directly underneath cadherin-rich periderm cell membranes—a phenomenon particularly prominent in the absence of axons (Supplemental Figure S5, A and B). When microdomains were compared within single basal cells from 1 dpf *ngn1* morphants, ordered microdomains had reduced dynamics compared with scattered ones (Supplemental Figure S5, C and D), suggesting that microdomains can be immobilized through homophilic interactions at cadherin-rich membranes in the absence of axons. Thus, axons promote the remodeling of basal cell surfaces by preventing ectopic association of lipid microdomains with cadherin-containing periderm membranes.

To test the third prediction—that lipid microdomains in basal cells align with lipid microdomains in periderm cells—we simultaneously labeled Lo membrane in periderm cells using a periderm-specific Tg(*krt5*:mp-mCherry) reporter and PIP2 in basal cells using Tg(*tp63*:GAL4VP16; UAS:EGFP-PLCδ-PH) (Figure 8, A and B). In 3 dpf larvae injected with *ngn1* MO, ~50–100% of all stable microdomains on the apical-facing surface of basal cells associated with microdomains enriched in mp-mCherry on the basal surface of periderm cells ($n = 56$ cell pairs from four embryos) (Figure 8, B–E).

To directly quantify periderm–basal cell junctions, we analyzed previously generated transmission electron microscopy (TEM) data sets of WT control and *ngn1* morphants (O'Brien *et al.*, 2012). Periderm–basal cell boundaries were followed in TEM sections in 54 hpf larvae. Junctions were scored as discrete electron-dense plaques on opposing periderm and basal membranes, with intervening electron density in the intermembrane space. We found an increased density of ultrastructurally defined junctions at periderm–basal boundaries in the absence of cutaneous axons versus WT controls (Figure 8, F–H). These data indicate that cutaneous axons remodel epithelial contacts during skin innervation, sequestering junction proteins at ensheathment channels that would otherwise contribute to interkeratinocyte adhesion. We propose that basal keratinocytes recruit and sequester junction components into lipid microdomains that function as versatile adhesion platforms to maintain the proper balance between axon ensheathment and epithelial adhesion.

DISCUSSION

Using live imaging of the larval zebrafish epidermis, we have found that cutaneous axon endings remodel lipids, actin, and junctions in basal keratinocytes. Our experiments demonstrate that epithelial cell membranes are not passive substrates that growth cones crawl over, but rather respond dynamically to axon contacts: Axons capture and create membrane microdomains of distinct lipid composition, promote the formation of dynamic F-actin–based protrusions, and concentrate cell adhesion molecules to facilitate a complex morphogenetic event.

Axon–epithelial cell interactions are selective

Although growing axons directly contact both periderm and basal keratinocyte membranes, we found that they dramatically reorganize the apical surface of basal keratinocytes but affect the basal surface of periderm cells much less. These cell type–specific responses may result from differences between the lipids in apical and basal epithelial membranes (Sampaio *et al.*, 2011; Cao *et al.*, 2012; Gerl *et al.*, 2012), different receptor proteins expressed by each cell type (Cokus *et al.*, 2019), or distinct mechanical properties, with apical membranes of basal cells being more deformable by axons than stiffer basal surfaces of periderm cells.

Reciprocally, some axons fail to induce basal cell microdomain formation or reorganization, even in the vicinity of axons that dramatically induced membrane remodeling. This selectivity precedes the formation of ensheathment channels around some axon segments but not others (Jiang *et al.*, 2019). The cues mediating specific axon recognition remain to be determined, but differential expression of cell surface cues on axonal membranes, or differences in mechanical properties of axonal segments, could play a role.

Axons induce the reorganization of epithelial membranes

Previous work demonstrated that axon contact promotes the formation of microdomains on basal epithelial cells within minutes (Jiang *et al.*, 2019). In this study, live time-lapse imaging revealed two mechanisms of microdomain formation. First, preexisting PIP2-enriched lipid microdomains coalesced to form larger, elongated domains beneath axons. In the absence of axons, the PIP2 reporter was present in patches, but these microdomains moved randomly within the membrane, indicating that axons induce their reorganization. In the second mechanism, PIP2-enriched microdomains appeared to extend from cell borders. Both mechanisms imply that axon cell surface properties rapidly induce remodeling of epithelial cell membranes, likely through interactions with cell surface receptors. Because only some axon segments induced basal cell microdomain remodeling, and protrusions in these microdomains formed largely around axon shafts and not growth cones, neurite-induced epithelial remodeling must act in a highly local manner, differing even along the length of a neurite. This localized mechanism could explain why ensheathment, which occurs over several days following axon growth, is neuron- and branch-specific.

Axon-associated microdomains have a distinct lipid composition

Membrane microdomains with a unique lipid composition had been proposed to be precursors of epidermal ensheathment channels, based on the observation that PIP2 reporters are enriched in both

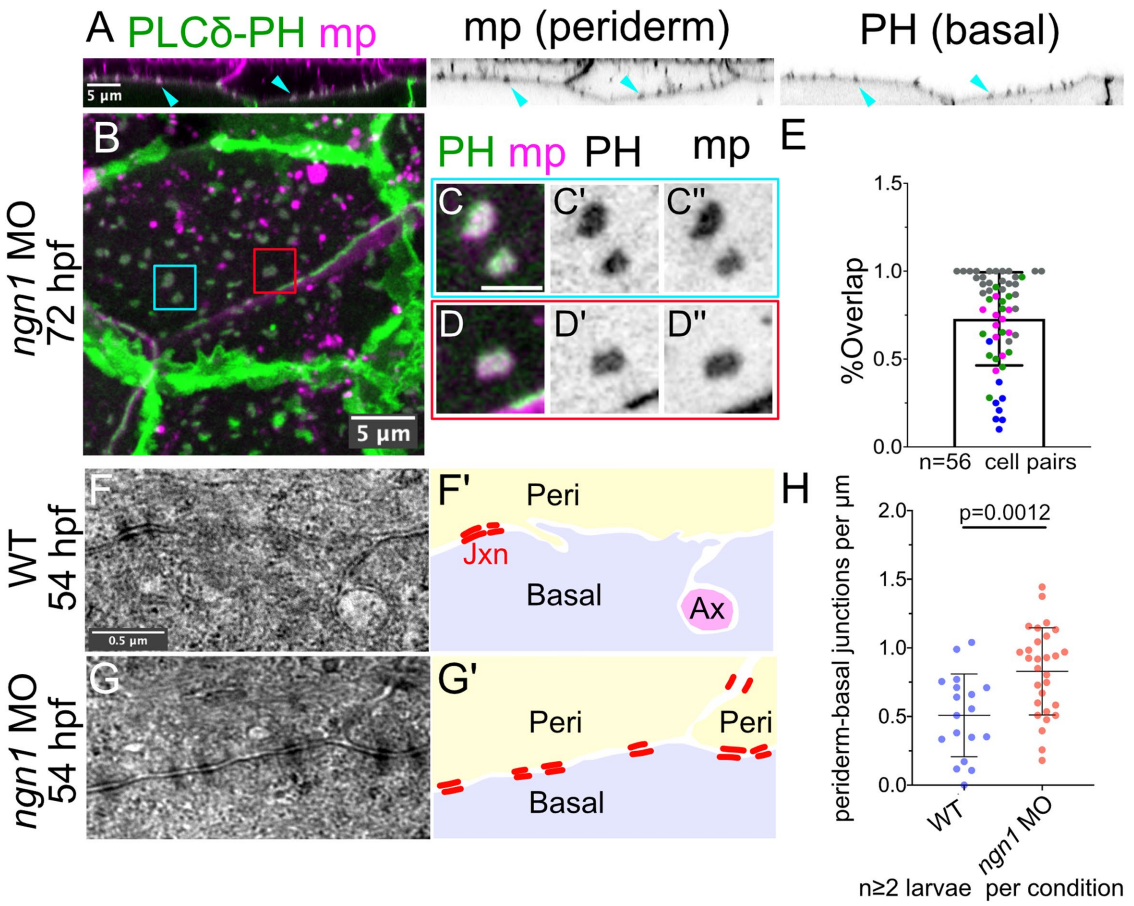

FIGURE 8: Axons inhibit the formation of periderm–basal cell junctions. (A) Periderm membrane (magenta) was specifically labeled using the krt5 promoter (Tg(*krt5*:mp-mCherry)), and basal membrane (green) was specifically labeled using the *tp63*:GAL4VP16 driver (Tg(*tp63*:GAL4VP16*;* UAS:EGFP-PLCδ-PH)) in larvae injected with *ngn1* MO to block sensory neuron development. Images show *xz* view of the entire epidermis. Arrowheads show examples of overlapping microdomains at the periderm–basal boundary. (B–D″) En face view of another periderm–basal boundary in a maximum-intensity projection. Boxes (C–D″) show examples of overlapping lipid microdomains at the periderm–basal boundary. (E) Quantification of the proportion of basal cell microdomains that overlapped with periderm microdomains. Each dot ($n = 56$) represents an independent basal–periderm cell pair, measured in four larvae. In three out of four larvae (gray, pink, magenta dots), ~50–100% of lipid microdomains in the two epithelial layers overlapped; in one larva (blue dots), <50% of lipid microdomains in the two skin layers overlapped, possibly due to differences in timing of junction maturation or developmental delay. An average of 24 microdomains were scored per cell pair. (F–G′) Representative TEM images of periderm–basal interfaces in 54 hpf WT (F) or *ngn1* morphants (*ngn1* MO, G). Junctions were identified as electron-dense plaques at the membrane (red bars in schematics on right). In WT epidermis, periderm–basal cell junctions were observed alongside wrapped axons (Ax in schematic). (H) Quantification of the density of periderm–basal junction plaques in WT and *ngn1* morphant TEM skin sections. In the absence of axons, the density of ultrastructurally defined periderm–basal junctions increased ($p = 0.0012$, unpaired *t* test). Each data point represents a unique region of the epidermis from at least two larvae per condition.

fish and fly neurite-associated domains (Jiang *et al.*, 2019). However, without comparing this reporter to other membrane reporters, it was not possible to distinguish whether these domains are biochemically distinct or simply contain more membrane. Here we provide quantitative evidence that axons promote the remodeling of epithelial membranes to create microdomains: A PIP2 reporter was more enriched than a prenylated membrane reporter (mRuby-CAAX), implying that accumulation of the PIP2 reporter in these domains is not explained simply by the presence of more membrane. This accumulation likely facilitates ensheathment, because inhibiting PIP2 production in *Drosophila* prevents neurite ensheathment by epidermal cells (Jiang *et al.*, 2019).

In diverse contexts, membrane lipids at cell–cell interfaces, and at specialized membrane structures, exhibit a unique composition. For example, the formation of immune synapses, specialized junctions between antigen-presenting cells and antibody-producing cells, requires the recruitment of signal transduction machinery into cholesterol- and sphingolipid-enriched Lo membranes (Dupre *et al.*, 2002; Hiltbold *et al.*, 2003; Nika *et al.*, 2006; Zuidscherwoude *et al.*, 2014). Clustering cell surface receptors within these membrane domains is essential for signaling (Miceli *et al.*, 2001; Cambi *et al.*, 2006; Jaumouille *et al.*, 2014; Martinez-Munoz *et al.*, 2018). To determine whether similar Lo domains facilitate axon–epithelial cell communication, we measured the relative enrichment of membrane reporters that preferentially associate with Lo or Ld membranes. Indeed, at every developmental stage, Lo reporters were enriched over Ld reporters at axon contact sites, and this enrichment increased as axon–epithelial contacts matured.

PIP2- and Lo-enriched, axon-associated domains form during initial axon contact, and a subset of axon-associated microdomains give rise to ensheathment channels. We propose that Lo membranes facilitate ensheathment channel formation in several ways. First, similar to immune synapses, they may concentrate signaling molecules that enable cell type–specific recognition between axons and epithelial cells. Second, a distinct lipid environment may promote membrane curvature around axons—Lo membranes are associated with highly curved membrane structures, including caveolae (Lamaze *et al.*, 2017), viral budding sites (Sengupta *et al.*, 2019), filopodia (Scorticati *et al.*, 2011), and myelin sheaths (Yurlova *et al.*, 2011). At viral budding sites, membrane curvature requires the partitioning of Lo-enriched membrane (Sengupta *et al.*, 2019). Finally, Lo membranes may recruit proteins that carry out later steps of axon ensheathment, including F-actin binding and junction proteins. Thus, membrane microdomains have the potential to orchestrate several activities that culminate in the formation of axon ensheathment channels.

Axon-associated lipid microdomains are sites of F-actin protrusion

In previous work, we found that F-actin reporters accumulate at ensheathment channels in both flies and zebrafish (Jiang *et al.*, 2019). In this study, we found that F-actin associates dynamically with PIP2-enriched, axon-associated microdomains at much earlier stages—soon after axons contact epithelial cells—and forms dynamic protrusions that selectively wrap around axons. Because several actin regulatory proteins, including Rho family GTPases, associate with PIP2 (Janmey *et al.*, 2018), we propose that PIP2 enrichment at these microdomains promotes actin polymerization. Our observation that PIP2 microdomains interact with both growth cones and axon shafts, whereas F-actin protrusions formed largely around axon shafts, suggests a stepwise maturation of axon-associated microdomains.

F-actin protrusions likely facilitate the wrapping of axons by basal cell membranes to form ensheathment channels but may play additional roles at axon-contact sites. For example, the coalescence of signaling complexes and membrane microdomains at immune synapses is actin dependent (Dupre *et al.*, 2002; Bolger-Munro *et al.*, 2019). Similarly, F-actin dynamics may promote the coalescence of microdomains below axons to cluster proteins involved in axon–skin cell signaling and/or ensheathment channel formation. F-actin protrusions may also contribute to membrane invagination around axons and, later, likely associate with autotypic adherens junctions.

Axon-associated lipid microdomains enrich junction components at ensheathment channels

We identified epithelial cadherins as one class of membrane proteins enriched in basal cell lipid microdomains. These microdomains progressively recruit cadherins as they mature, even in the absence of axons. Thus, axons do not themselves attract epithelial cadherins but rather promote the remodeling of independently formed, cadherin-enriched microdomains.

Actin-based protrusions containing cadherins initiate adherens junction formation between keratinocytes (adhesion zippers; Vasioukhin *et al.*, 2000) and maintain stable adhesions by interdigitating membranes (microspikes; Li *et al.*, 2020), suggesting that the protrusions we see at sites of axon contact may be related to those structures. As axons grow in the epidermis, dynamic lipid microdomains make transient contacts with periderm membranes and axons. Around axons, adhesion zipper–like structures might promote adhesion of invaginating membranes as they wrap around axons, forming an autotypic adherens junction, whereas microdomains that do not associate with axons mature into stable periderm–basal cell adhesions.

The enrichment of PIP2 and raft-associated reporters at maturing ensheathment channels could be both a cause and a consequence of cadherin recruitment to axon-associated membrane domains. During epithelial and axo–glial junction formation, junction-associated proteins increasingly associate with Lo membrane (Honke *et al.*, 2002; Schafer *et al.*, 2004; Susuki *et al.*, 2007; Resnik *et al.*, 2011; Guillaume *et al.*, 2013; Kurrle *et al.*, 2013; Stahley *et al.*, 2014; Lewis *et al.*, 2019). For some membrane proteins, such as the desmosomal cadherin Desmoglein, partitioning into Lo membrane is essential for proper junction formation (Lewis *et al.*, 2019). Thus, we hypothesize that Lo membrane enrichment at axon-associated membrane domains is required for autotypic junction formation. Cadherin clustering in cholesterol- and sphingolipid-enriched membranes could provide a sorting cue at the *trans*-Golgi network for cadherins (Cao *et al.*, 2012), promoting their targeting to microdomains, and a highly ordered lipid environment could promote the lateral clustering of cadherins, increasing the avidity of *trans* cadherin interactions to promote junction formation (Zhang *et al.*, 2009). The stronger enrichment in early microdomains of Desmocollin-2–like compared with E-cad may reflect a stronger or more direct involvement of lipid sorting for the desmosomal cadherin (Lewis *et al.*, 2019).

Our study suggests several possible functions for axon-induced reorganization of lipid microdomains with a unique lipid composition, including cadherin enrichment, F-actin accumulation, and axon wrapping. These ideas could be tested by conditional or cell type–specific knockout of cholesterol or sphingolipid biosynthetic machinery. Increasing evidence suggests that the physical association of keratinocyte membranes with nociceptive nerve endings plays direct roles in neurite branching and sensory transduction (Sondersorg *et al.*, 2014; Baumbauer *et al.*, 2015; Pang *et al.*, 2015; Moehring *et al.*, 2018). Lipid microdomains may function as a means of compartmentalizing this machinery in keratinocyte membranes for future recruitment to axons. Subsequent work will seek to identify signaling molecules recruited to microdomains and their functions in axon ensheathment and sensory transduction.

Most epithelial surfaces in our body are innervated, yet most studies on epithelial junction maturation involve systems devoid of sensory neurites. Signals from parasympathetic and sympathetic neurons regulate multiple steps of epithelial tubulogenesis, including branch formation (Bower *et al.*, 2014; Nedvetsky *et al.*, 2014) and apical membrane expansion (Nedvetsky *et al.*, 2014). While previous work has focused on the role of neurotransmission and secreted peptides on epithelial morphogenesis—in some cases affecting epithelial properties through non–cell autonomous processes (Magnon *et al.*, 2013)—our study demonstrates how neurites influence basic epithelial properties through direct physical interactions. By determining the distribution of lipids, cytoskeletal elements, and cadherins, axons regulate the distribution of cellular components whose polarized localization is critical for epithelial morphogenesis and homeostasis and may thus have profound consequences on mechanical properties and signaling in epithelia.

MATERIALS AND METHODS

Request a protocol through *Bio-protocol*.

Zebrafish husbandry and microinjections

Zebrafish (*Danio rerio*) were raised at 28.5°C on a 14-h/10-h light/dark cycle. Embryos were raised at 28.5°C in embryo water

composed of 0.3 g/l Instant Ocean salt (Spectrum Brands) and 0.1% methylene blue. Zebrafish lines used were Tg(*tp63*:GAL4VP16; UAS:EGFP-PLCδ-PH) (Rasmussen *et al.*, 2015); Tg(*krt5:GAL4*) (Rasmussen *et al.*, 2015); Tg(*tp63*:GAL4VP16; UAS: LifeAct-GFP) (Rasmussen *et al.*, 2015); *cdh1*-TdTomato (Cronan *et al.*, 2018); Tg(*krt5*:myrpalm-mCherry) (this work); Tg(*isl1*:GAL4VP16; UAS:EGFP) (Rasmussen *et al.*, 2015); Tg(*isl1*:LexA; LexAop:TdTomato) (Rasmussen *et al.*, 2015); and Tg(*neural beta tubulin:DsRed*) (Peri and Nüsslein-Volhard, 2008).

Fertilized eggs were collected at the one-cell stage for injections. Approximately one nanogram of the *ngn1* MO (5′-ACGATCTC-CATTGTTGATAACCTGG-3′; Andermann *et al.*, 2002) or a standard negative control morpholino (5′-CTCTTACCTCAGTTACAATT-TATA-3′; GeneTools) was injected into the yolk. Morpholinos were diluted in autoclaved double-deionized water to working concentrations of 1 ng/nl. For plasmid DNA injections, ~15–20 pg of DNA was coinjected with ~25 pg of *tol2* mRNA to facilitate recovery of somatic clones. Injection volumes were calibrated in drops of mineral oil on a slide micrometer.

Molecular biology

Generation of Lo and Ld membrane reporters. The myrpalm (mp) reporters were constructed according to sequences described in Zacharias *et al.*, (2002). Briefly, a forward primer containing the sequence 5′-CATGGGATGTATTAATAGTAAGCGAAAGGAT-(gene-specific sequence)-3′ was used to add the consensus sequence for the myristoylation and palmitoylation modifications at the N-terminus of the coding sequences for mEGFP, mApple, and mCherry, followed by TA cloning into pCRII-TOPO. cDNAs encoding the myrpalm-modified fluorescent proteins were subcloned into pDONR221-MCS-T2A for use in the Gateway cloning system (Kwan *et al.*, 2007). See Supplemental Methods table for a list of primers and plasmids used for cloning.

To make mp-mEGFP (A206K, L221K, L223K), site-directed mutagenesis was performed on pCRII-mp-EGFP using a QuikChange Lightning mutagenesis kit (Agilent) to introduce two further mutations, L221K and L223K, which eliminate any tendency of EGFP (A206K) to oligomerize. See Supplemental Methods table for a list of primers and plasmids used for cloning.

To generate a GPI-anchored reporter, a codon-optimized signal sequence from human ER-resident p23 was inserted into the *Age*I site of p-sfGFP-N1 (Addgene #54737). p23ss-sfGFP lacking the stop codon was PCR amplified and flanked with a 3′ *Nhe*I site and TA cloned into the pCRII-TOPO vector. The introduced *Nhe*I site and a backbone *Eco*RV site in pCRII-TOPO were used to insert a codon-optimized C-terminal GPI signal from rat Neurotrimin (Uniprot Identifier NTRI_rat; amino acid sequence: N-AVSE-VNNGTSRRAGCIWLLPLLVLHLLLKF*-C) (Galian *et al.*, 2012). The resultant full-length p23ss-sfGFP-GPI was then inserted into pDONR221-MCS-T2A. See Supplemental Methods table for a list of primers and plasmids used for cloning.

To label Ld membrane, a codon-optimized signal sequence with an N-terminal G_5S linker sequence (encoding: N-DGKKKKKK-SKTKCNLL*-C, derived from the Rap1b CAAX box) (Pyenta *et al.*, 2001; Sengupta *et al.*, 2019) was added to the C-terminus of mEGFP or mApple. mEGFP-gg and mApple-gg coding sequences were flanked with 5′ attB2r and 3′ attB3 recognition sequences to make p3E-mEGFP-gg and p3E-mApple-gg entry clones. See Supplemental Methods table for a list of primers and plasmids used for cloning.

Sequence-validated pME-mp-mApple-T2A, pME-mp-mEGFP-T2A, and pME-p23ss-sfGFP-GPI clones were then used in LR Gateway recombination reactions with p5E-10xUAS or p5e-krtt1c19e (Rasmussen *et al.*, 2015), and p3E-mEGFP-gg or p3E-mApple-gg, into the pDestTol2CG destination vector (Kwan *et al.*, 2007). The p5E-krtt1c19e entry clone contains a promoter fragment from the *keratin type 1 c19e* gene that drives expression in basal keratinocytes (Rasmussen *et al.*, 2015). A Kozak sequence (GCCGC-CACCATGG) was included around the start codons for all expression constructs.

Generation of dual EGFP-PLCδ-PH membrane reporters. A HindIII-EGFP-PLCδ-PH-KpnI fragment was PCR amplified and subcloned into pDONR221-MCS-T2A. The resultant pME-EGFP-PLCδ-PH-T2A plasmid was used with p5E-10XUAS (Kwan *et al.*, 2007), p3E-mRubyCAAX (Kwan *et al.*, 2007), or p3E-mApple-gg in LR recombination reactions into the destination vector pDestTol2CG. See Supplemental Methods table for primers used.Competent *Escherichia coli* was grown in LB broth supplemented with antibiotics under standard conditions. Plasmid DNA was purified using Qiagen Mini Prep kits. For purification of Dsc2l-GFP Bacterial Artificial Chromosome, a NucleoSnap Plasmid Midi kit (Takara Bio) was used. PCRs were carried out using Phusion DNA polymerase or Taq DNA Polymerase and commercial buffers (New England Biolabs). Reactions were run on a BioRad C1000 Touch thermal cycler. PCR products were either cleaned up using DNA Clean & Concentrator kits (Zymo Research) or gel purified using a Gel Purification kit (Zymo Research). Plasmid DNA was transformed into OneShot Top10 competent cells (Invitrogen). Oligonucleotides were synthesized by Integrated DNA Technologies.

Generation of Tg(*krt5*:mp-mCherry) transgenic fish

An attB1-mp-mCherry-attB2 PCR product was recombined into the pDONR221 vector. The resultant pME-mp-mCherry was used in a LR Gateway recombination reaction in combination with p5E-*krt5*, p3E-polyA entry clones, and the pDestTol2CG destination vector. pDest-*krt5*:mp-mCherry-polyA (~15 pg) was coinjected with ~20 pg of *tol2* mRNA into the ooplasm of WT AB oocytes at the one-cell stage. F0 adults were crossed to WT fish to screen for founder fish that segregated mp-mCherry expression in the periderm of the F1s. Five founders were identified to establish transgenic lines. For the experiments described in this paper, a single founder with ~30% germline transmission was crossed to other transgenic lines for live imaging. See Supplemental Methods table for a list of primers used.

Microscopy and live imaging

For end-point imaging, live embryos or larvae were anesthetized in Tricaine and mounted in 1.2% low-melt agarose with their dorsal side against the coverslip to image the epidermis covering the head. Immobilized embryos were bathed in embryo water containing Tricaine within an imaging chamber formed by custom-made plastic rings sealed onto coverslips using vacuum grease (O'Brien *et al.*, 2009).

Confocal imaging was performed using a Zeiss LSM 880 microscope with 488 nm (<0.5–1% laser power) and 561 nm excitation lasers (1–2% laser power). Slides were mounted on a stage heater heated to 28.5°C. Z-stacks were acquired every 3–7 min for ~5–7 h. Movies were acquired using either a 20× air objective or 40× oil immersion objectives with 2–3× scan zoom. Z-volumes (~10–25 µm) were acquired using a 63× oil immersion objective and a 2–3× scan zoom.

Fast Airyscan imaging was performed using a Zeiss LSM 980 microscope with 488 nm (2–6% laser power) and 561 nm (8–10% laser power) excitation lasers. Faster acquisition speeds were obtained

with the multiplex 4Y "SR-4Y" mode by scanning four pixels in parallel. Higher spatial resolution (max 140 nm *x*/140 nm *y*/450 nm *z*) was obtained by opening the pinhole to collect all emitted light with a 32 detector array. Z-stacks were acquired every 20–30 s for ~1–3 h. Z-volumes (~7–10 µm) were acquired with a 63× oil immersion objective with a 2× scan zoom.

Cholesterol depletion with methyl-β-cyclodextrin

Individual 4 dpf Tg(*tp63*:GAL4VP16;UAS:EGFP-PLCδ-PH); *cdh1*-TdTomato embryos were placed in multiwell culture plates and incubated in 1 ml of vehicle (0.5% dimethyl sulfoxide [DMSO] in isotonic Ringer's), 5 mM MBCD (in 0.5% DMSO/Ringer's diluent; Cayman Chemical), or 10 mM MBCD (in 0.5% DMSO/Ringers diluent) solution for 10 min. Embryos were then anesthetized using Tricaine in embryo water for ~1 min. Embryos were rapidly mounted in 1.2% low-melt agarose and imaged by confocal microscopy using 488 and 561 nm excitation wavelengths. Z-stacks for each embryo were collected. MBCD solutions were prepared fresh the day of the experiment.

Image analysis

Image quantitation was done in ImageJ using maximum projected images. To quantify membrane reporter enrichment in microdomains and ensheathment channels, an ~1.5–2 µm linear region of interest (ROI) was drawn orthogonally across a microdomain or ensheathment channel to obtain intensity profiles. For the Lo and Ld reporters, the ratio of the maximum reporter intensity inside to the intensity outside the microdomain/ensheathment channel was used to estimate relative enrichment. See Figure 3B for illustration. More than five measurements were taken per basal cell clone. An identical approach was used to measure relative enrichment of Lo and Ld reporters in isolated microdomains. Relative enrichment values were averaged within individual clones to plot average relative intensities. To visualize cadherin recruitment to microdomains, intensity values along the linear ROI were normalized to the mean fluorescence intensity in a region encompassing both the microdomain and the surrounding nonmicrodomain membrane to produce plots of normalized intensities, allowing semiquantitative comparison of cadherin recruitment across hundreds of microdomains with different transgene expression levels.

To measure PIP2 membrane domain lengths, the SNT plug-in in ImageJ was used to trace and measure the length of PIP2 membrane domains in maximum-intensity projections of EGFP-PLCδ-PH–expressing periderm and basal cells. To accurately visualize basal PIP2 domains in the periderm, projections lacking the most apical regions of these cells were used.

To quantify PIP2 lipid microdomain dynamics, ~1-min-interval movies were made in 1 or 4 dpf Tg(*tp63*:GAL4VP16; UAS: EGFP-PLCδ-PH) zebrafish. To minimize image drift, movies were stabilized to the second frame with the ImageJ "Image Stabilizer" plug-in. PIP2-rich microdomains in basal cells of 1 and 4 dpf control and *neurogenin1* morphants were selected as ROI with the polygon tool. Selected ROIs were duplicated to another window, and cell borders were omitted from the analysis with the "Clear Outside" command. The brightness and contrast were automatically adjusted for the ROI and automatically thresholded with the "Default" algorithm. Frames within the movie were separated with the "Stack Splitter" command, and overlap coefficients between the first frame and subsequent frames were extracted with the "Just Another Colocalization Plugin" (JACoP) in ImageJ.

The sharp drop in overlap coefficient values between the first and second frames occurs because of the stochastic dynamics of lipid microdomains in all conditions. Owing to random fluctuations in the plasma membrane, there is a higher probability that fewer pixels will overlap than will stay the same between the first and second frames. As lipid microdomains shift over time, the probability that more pixels will overlap with the first frame increases, resulting in a gradual—rather than precipitous—decline in overlap coefficient values. The rate of this decline was uniform across all conditions, even when lipid microdomains mature into stable adhesions, most likely due to the fact that the intrinsic dynamics of the basal cell plasma membrane is not changing across the experimental variables.

Transmission electron microscopy

Generation of TEM data was described in O'Brien *et al*. (2012). The periderm–basal boundary was followed in TEM sections from ≥2 larvae per condition. Within a given image, the length of the periderm–basal boundary was traced and measured. The electron-dense junction plaques wete counted, and the number was normalized to the length of the periderm–basal boundary. Nineteen sections were quantified for WT control larvae and 29 for *ngn1* morphants.

Statistics

Statistical analysis was performed in Prism (v9.2.0) and R statistical software. Shapiro–Wilks tests were used to assess the normality of the distributions of data sets. One-way analysis of variance (ANOVA) or Kruskal–Wallis tests were used to compare the distributions across multiple time points, where appropriate. For pairwise comparisons of independent data, unpaired *t* tests or Mann–Whitney U tests were performed. For paired data, paired *t* tests or Wilcoxon signed rank tests were used. *P* values less than or equal to 0.05 were considered significantly different from the null hypothesis. See figure legends for specific statistical tests performed for each experiment.

ACKNOWLEDGMENTS

We thank Kaitlin Ching for comments on the manuscript, Jeff Long for access to Airyscan microscopy, and Son Giang and Linda Dong for excellent fish care. This work was funded by National Institutes of Health Dermatology T32 grant T32AR071307 to J.B.R. and National Institutes of Health grant R01AR064582 to A. S.

REFERENCES

Andermann P, Ungos J, Raible DW (2002). Neurogenin1 defines zebrafish cranial sensory ganglia precursors. Dev Biol 251, 45–58.

Baumbauer KM, DeBerry JJ, Adelman PC, Miller RH, Hachisuka J, Lee KH, Ross SE, Koerber HR, Davis BM, Albers KM (2015). Keratinocytes can modulate and directly initiate nociceptive responses. eLife 4, e09674.

Bolger-Munro M, Choi K, Scurll JM, Abraham L, Chappell RS, Sheen D, Dang-Lawson M, Wu X, Priatel JJ, Coombs D, *et al*. (2019). Arp2/3 complex-driven spatial patterning of the BCR enhances immune synapse formation, BCR signaling and B cell activation. eLife 8, e44574.

Bower DV, Lee HK, Lansford R, Zinn K, Warburton D, Fraser SE, Jesudason EC (2014). Airway branching has conserved needs for local parasympathetic innervation but not neurotransmission. BMC Biol 12, 92.

Cambi A, Joosten B, Koopman M, de Lange F, Beeren I, Torensma R, Fransen JA, Garcia-Parajo M, van Leeuwen FN, Figdor CG (2006). Organization of the integrin LFA-1 in nanoclusters regulates its activity. Mol Biol Cell 17, 4270–4281.

Cao X, Surma MA, Simons K (2012). Polarized sorting and trafficking in epithelial cells. Cell Res 22, 793–805.

Chalfie M, Sulston J (1981). Developmental genetics of the mechanosensory neurons of Caenorhabditis elegans. Dev Biol 82, 358–370.

Coakley S, Ritchie FK, Galbraith KM, Hilliard MA (2020). Epidermal control of axonal attachment via beta-spectrin and the GTPase-activating protein TBC-10 prevents axonal degeneration. Nat Commun 11, 133.

Cokus SJ, De La Torre M, Medina EF, Rasmussen JP, Ramirez-Gutierrez J, Sagasti A, Wang F (2019). Tissue-specific transcriptomes reveal gene expression trajectories in two maturing skin epithelial layers in zebrafish embryos. G3 9, 3439–3452.
Cronan MR, Matty MA, Rosenberg AF, Blanc L, Pyle CJ, Espenschied ST, Rawls JF, Dartois V, Tobin DM (2018). An explant technique for high-resolution imaging and manipulation of mycobacterial granulomas. Nat Methods 15, 1098–1107.
Dupre L, Aiuti A, Trifari S, Martino S, Saracco P, Bordignon C, Roncarolo MG (2002). Wiskott-Aldrich syndrome protein regulates lipid raft dynamics during immunological synapse formation. Immunity 17, 157–166.
Galian C, Bjorkholm P, Bulleid N, von Heijne G (2012). Efficient glycosylphosphatidylinositol (GPI) modification of membrane proteins requires a C-terminal anchoring signal of marginal hydrophobicity. J Biol Chem 287, 16399–16409.
Garcia-Parajo MF, Cambi A, Torreno-Pina JA, Thompson N, Jacobson K (2014). Nanoclustering as a dominant feature of plasma membrane organization. J Cell Sci 127, 4995–5005.
Gerl MJ, Sampaio JL, Urban S, Kalvodova L, Verbavatz JM, Binnington B, Lindemann D, Lingwood CA, Shevchenko A, Schroeder C, Simons K (2012). Quantitative analysis of the lipidomes of the influenza virus envelope and MDCK cell apical membrane. J Cell Biol 196, 213–221.
Guillaume E, Comunale F, Do Khoa N, Planchon D, Bodin S, Gauthier-Rouviere C (2013). Flotillin microdomains stabilize cadherins at cell-cell junctions. J Cell Sci 126, 5293–5304.
Han C, Wang D, Soba P, Zhu S, Lin X, Jan L Y, Jan YN (2012). Integrins regulate repulsion-mediated dendritic patterning of drosophila sensory neurons by restricting dendrites in a 2D space. Neuron 73, 64–78.
Hiltbold EM, Poloso NJ, Roche PA (2003). MHC class II-peptide complexes and APC lipid rafts accumulate at the immunological synapse. J Immunol 170, 1329–1338.
Honda A, Ito Y, Takahashi-Niki K, Matsushita N, Nozumi M, Tabata H, Takeuchi K, Igarashi M (2017). Extracellular signals induce glycoprotein M6a clustering of lipid rafts and associated signaling molecules. J Neurosci 37, 4046–4064.
Honke K, Hirahara Y, Dupree J, Suzuki K, Popko B, Fukushima K, Fukushima J, Nagasawa T, Yoshida N, Wada Y, Taniguchi N (2002). Paranodal junction formation and spermatogenesis require sulfoglycolipids. Proc Natl Acad Sci USA 99, 4227–4232.
Janmey PA, Bucki R, Radhakrishnan R (2018). Regulation of actin assembly by PI(4,5)P2 and other inositol phospholipids: an update on possible mechanisms. Biochem Biophys Res Commun 506, 307–314.
Jaumouille V, Farkash Y, Jaqaman K, Das R, Lowell CA, Grinstein S (2014). Actin cytoskeleton reorganization by Syk regulates Fcgamma receptor responsiveness by increasing its lateral mobility and clustering. Dev Cell 29, 534–546.
Jiang N, Rasmussen JP, Clanton JA, Rosenberg MF, Luedke KP, Cronan MR, Parker ED, Kim HJ, Vaughan JC, Sagasti A, Parrish JZ (2019). A conserved morphogenetic mechanism for epidermal ensheathment of nociceptive sensory neurites. eLife 8, e42455.
Kim JH, Lee S-R, Li L-H, Park H-J, Park J-H, Lee KY, Kim M-K, Shin BA, Choi S-Y (2011). High cleavage efficiency of a 2A peptide derived from porcine teschovirus-1 in human cell lines, zebrafish and mice. PLoS One 6, e18556.
Kim ME, Shrestha BR, Blazeski R, Mason CA, Grueber WB (2012). Integrins establish dendrite-substrate relationships that promote dendritic self-avoidance and patterning in drosophila sensory neurons. Neuron 73, 79–91.
Kurrle N, Vollner F, Eming R, Hertl M, Banning A, Tikkanen R (2013). Flotillins directly interact with gamma-catenin and regulate epithelial cell-cell adhesion. PLoS One 8, e84393.
Kwan KM, Fujimoto E, Grabher C, Mangum BD, Hardy ME, Campbell DS, Parant JM, Yost HJ, Kanki JP, Chien C-B (2007). The Tol2kit: a multisite gateway-based construction kit for Tol2 transposon transgenesis constructs. Dev Dyn 236, 3088–3099.
Lamaze C, Tardif N, Dewulf M, Vassilopoulos S, Blouin CM (2017). The caveolae dress code: structure and signaling. Curr Opin Cell Biol 47, 117–125.
Lewis JD, Caldara AL, Zimmer SE, Stahley SN, Seybold A, Strong NL, Frangakis AS, Levental I, Wahl JK 3rd, Mattheyses AL *et al.* (2019). The desmosome is a mesoscale lipid raft-like membrane domain. Mol Biol Cell 30, 1390–1405.
Li JXH, Tang VW, Brieher WM (2020). Actin protrusions push at apical junctions to maintain E-cadherin adhesion. Proc Natl Acad Sci USA 117, 432–438.
Magnon C, Hall SJ, Lin J, Xue X, Gerber L, Freedland SJ, Frenette PS (2013). Autonomic nerve development contributes to prostate cancer progression. Science 341, 1236361.
Martinez-Munoz L, *et al.* (2018). Separating actin-dependent chemokine receptor nanoclustering from dimerization indicates a role for clustering in CXCR4 signaling and function. Mol Cell 70, 106–119.e10.
Miceli MC, Moran M, Chung CD, Patel VP, Low T, Zinnanti W (2001). Co-stimulation and counter-stimulation: lipid raft clustering controls TCR signaling and functional outcomes. Semin Immunol 13, 115–128.
Mikesell AR, Isaeva O, Moehring F, Sadler KE, Menzel AD, Stucky CL (2022). Keratinocyte PIEZO1 modulates cutaneous mechanosensation. eLife 11, e65987.
Moehring F, Cowie AM, Menzel AD, Weyer AD, Grzybowski M, Arzua T, Geurts AM, Palygin O, Stucky CL (2018). Keratinocytes mediate innocuous and noxious touch via ATP-P2X4 signaling. eLife 7, e31684.
Nedvetsky PI, Emmerson E, Finley JK, Ettinger A, Cruz-Pacheco N, Prochazka J, Haddox CL, Northrup E, Hodges C, Mostov KE, *et al.* (2014). Parasympathetic innervation regulates tubulogenesis in the developing salivary gland. Dev Cell 30, 449–462.
Nika K, Charvet C, Williams S, Tautz L, Bruckner S, Rahmouni S, Bottini N, Schoenberger SP, Baier G, Altman A, *et al.* (2006). Lipid raft targeting of hematopoietic protein tyrosine phosphatase by protein kinase C theta-mediated phosphorylation. Mol Cell Biol 26, 1806–1816.
O'Brien GS, Rieger S, Martin SM, Cavanaugh AM, Portera-Cailliau C, Sagasti A (2009). Two-photon axotomy and time-lapse confocal imaging in live zebrafish embryos. J Vis Exp 2009, 1129.
O'Brien GS, Rieger S, Wang F, Smolen GA, Gonzalez RE, Buchanan J, Sagasti A (2012). Coordinate development of skin cells and cutaneous sensory axons in zebrafish. J Comp Neurol 520, 816–831.
Pang Z, Sakamoto T, Tiwari V, Kim YS, Yang F, Dong X, Guler AD, Guan Y, Caterina MJ (2015). Selective keratinocyte stimulation is sufficient to evoke nociception in mice. Pain 156, 656–665.
Peri F, Nüsslein-Volhard C (2008). Live imaging of neuronal degradation by microglia reveals a role for v0-ATPase a1 in phagosomal fusion in vivo. Cell 133, 916–927.
Pyenta PS, Holowka D, Baird B (2001). Cross-correlation analysis of inner-leaflet-anchored green fluorescent protein co-redistributed with IgE receptors and outer leaflet lipid raft components. Biophys J 80, 2120–2132.
Rasmussen JP, Sack GS, Martin SM, Sagasti A (2015). Vertebrate epidermal cells are broad-specificity phagocytes that clear sensory axon debris. J Neurosci 35, 559–570.
Resnik N, Sepcic K, Plemenitas A, Windoffer R, Leube R, Veranic P (2011). Desmosome assembly and cell-cell adhesion are membrane raft-dependent processes. J Biol Chem 286, 1499–1507.
Sagasti A, Guido MR, Raible DW, Schier AF (2005). Repulsive interactions shape the morphologies and functional arrangement of zebrafish peripheral sensory arbors. Curr Biol 15, 804–814.
Sampaio JL, Gerl MJ, Klose C, Ejsing CS, Beug H, Simons K, Shevchenko A (2011). Membrane lipidome of an epithelial cell line. Proc Natl Acad Sci USA 108, 1903–1907.
Schafer DP, Bansal R, Hedstrom KL, Pfeiffer SE, Rasband MN (2004). Does paranode formation and maintenance require partitioning of neurofascin 155 into lipid rafts? J Neurosci 24, 3176–3185.
Scorticati C, Formoso K, Frasch AC (2011). Neuronal glycoprotein M6a induces filopodia formation via association with cholesterol-rich lipid rafts. J Neurochem 119, 521–531.
Sengupta P, Seo AY, Pasolli HA, Song YE, Johnson MC, Lippincott-Schwartz J (2019). A lipid-based partitioning mechanism for selective incorporation of proteins into membranes of HIV particles. Nat Cell Biol 21, 452–461.
Sondersorg AC, Busse D, Kyereme J, Rothermel M, Neufang G, Gisselmann G, Hatt H, Conrad H (2014). Chemosensory information processing between keratinocytes and trigeminal neurons. J Biol Chem 289, 17529–17540.
Stahley SN, Saito M, Faundez V, Koval M, Mattheyses AL, Kowalczyk AP (2014). Desmosome assembly and disassembly are membrane raft-dependent. PLoS One 9, e87809.
Susuki K, Baba H, Tohyama K, Kanai K, Kuwabara S, Hirata K, Furukawa K, Furukawa K, Rasband MN, Yuki N (2007). Gangliosides contribute to stability of paranodal junctions and ion channel clusters in myelinated nerve fibers. Glia 55, 746–757.
Talagas M, Lebonvallet N, Leschiera R, Sinquin G, Elies P, Haftek M, Pennec JP, Ressnikoff D, La Padula V, Le Garrec R, *et al.* (2020a). Keratinocytes communicate with sensory neurons via synaptic-like contacts. Ann Neurol 88, 1205–1219.

Talagas M, Lebonvallet N, Leschiera R, Elies P, Marcorelles P, Misery L (2020b). Intra-epidermal nerve endings progress within keratinocyte cytoplasmic tunnels in normal human skin. Exp Dermatol 29, 387–392.
Tenenbaum CM, Misra M, Alizzi RA, Gavis ER (2017). Enclosure of dendrites by epidermal cells restricts branching and permits coordinated development of spatially overlapping sensory neurons. Cell Rep 20, 3043–3056.
Vasioukhin V, Bauer C, Yin M, Fuchs E (2000). Directed actin polymerization is the driving force for epithelial cell-cell adhesion. Cell 100, 209–219.
Wu H, Williams J, Nathans J (2012). Morphologic diversity of cutaneous sensory afferents revealed by genetically directed sparse labeling. eLife 1, e00181.
Yang WK, Chueh YR, Cheng YJ, Siegenthaler D, Pielage J, Chien CT (2019). Epidermis-derived L1CAM homolog neuroglian mediates dendrite enclosure and blocks heteroneuronal dendrite bundling. Curr Biol 29, 1445–1459.e3.
Yin C, Peterman E, Rasmussen JP, Parrish JZ (2021). Transparent touch: insights from model systems on epidermal control of somatosensory innervation. Front Cell Neurosci 15, 680345.
Yoshino J, Mali SS, Williams CR, Morita T, Emerson CE, Arp CJ, Miller SE, Yin C, Lydia Thé, Hemmi C, *et al*. (2022). Drosophila epidermal cells are intrinsically mechanosensitive and drive nociceptive behavioral outputs. bioRxiv https://doi.org/10.1101/2022.10.07.511265.
Yurlova L, Kahya N, Aggarwal S, Kaiser HJ, Chiantia S, Bakhti M, Pewzner-Jung Y, Ben-David O, Futerman AH, Brugger B, *et al*. (2011). Self-segregation of myelin membrane lipids in model membranes. Biophys J 101, 2713–2720.
Zacharias DA, Violin JD, Newton AC, Tsien RY (2002). Partitioning of lipid-modified monomeric GFPs into membrane microdomains of live cells. Science 296, 913–916.
Zhang Y, Sivasankar S, Nelson WJ, Chu S (2009). Resolving cadherin interactions and binding cooperativity at the single-molecule level. Proc Natl Acad Sci USA 106, 109–114.
Zidovetzki R, Levitan I (2007). Use of cyclodextrins to manipulate plasma membrane cholesterol content: evidence, misconceptions and control strategies. Biochim Biophys Acta 1768, 1311–1324.
Zuidscherwoude M, de Winde CM, Cambi A, van Spriel AB (2014). Microdomains in the membrane landscape shape antigen-presenting cell function. J Leukoc Biol 95, 251–263.
Zylka MJ, Rice FL, Anderson DJ (2005). Topographically distinct epidermal nociceptive circuits revealed by axonal tracers targeted to Mrgprd. Neuron 45, 17–25.